A Nanoindentation Device and the Scale-Dependent Mechanical Properties of Native and Decellularized Liver Tissue

By

Douglas W. Evans

A Thesis Submitted to the Graduate Faculty of
VIRGINIA TECH – WAKE FOREST UNIVERSITY
SCHOOL OF BIOMEDICAL ENGINEERING & SCIENCES

In Partial Fulfillment of the Requirements

for the Degree of

MASTER OF SCIENCE

Biomedical Engineering

December 2011

Winston-Salem, North Carolina

Approved by:

Jessica L. Sparks, PhD, Advisor, Chair

Examining Committee:

Keith Bonin, PhD

Joel D. Stitzel, PhD

Acknowledgements

I would like to thank my advisor Dr. Jessica Sparks and the past and present members of the Soft Tissue Biomechanics Lab, Emma Moran, Smitha Ragunathan, and Nicholas Vavalle. I also want to thank Phillip Brown for his machining expertise and Anthony Santago for his vast computer programming knowledge. Last and certainly not least, I thank my family and friends for their support and encouragement throughout the years.

Table of Contents

List of Tables

List of Figures

Abstract

Regenerative medicine is an emerging field with the goal of treating disease with engineered replacements for cells, tissues, and organs. One technique in regenerative medicine is decellularization, the removal of the native cells from an organ leaving behind an intact structure of extracellular material to act as a scaffold for new cells. Characterizing the biomechanical properties of these scaffolds is important due to the mechanosensitivity of many cell types. In addition, in the emerging field of multi-scale modeling an effort is being made to integrate the small fundamental scales with the large functional scales that exist in the hierarchial structure of biological systems. The aim of this work was to investigate and quantify the biomechanical properties of perfused decellularized liver scaffolds and compare them to perfused native tissue properties on both a macro and nano-scale. To accomplish this goal, a novel Nano-Tissue Indenter (NTI) was constructed that can be used to perform nanoindentation on virtually any soft biologic tissue or biomaterial. The device was validated by comparing its measurements with results obtained through traditional unconfined compression testing. The NTI was used along with conventional macro-indentation to evaluate mechanical property differences in native and decellularized liver at the tissue and cellular-scales. A poroviscoelastic (PVE) finite element model was employed to capture the solid and fluid components of liver material behavior. The end result of this work was the first characterization of the biomechanical properties of perfused decellularized liver tissue and how it differs from perfused native tissue measured by spherical macro and nanoindentation.

Chapter I

1. Introduction and Background

1.1 *Regenerative Medicine/Tissue Engineering*

Simply put, "regenerative medicine replaces or regenerates human cells, tissue, or organs, to restore or establish normal function"[1]. Between 2006 and 2010 there were about 28,500 organ transplantations performed yearly across the United States, yet the list of candidates awaiting organs remains at approximately 100,000 every year[2]. With advances in tissue engineering, such as the successful fabrication and transplantation of a bladder [3], the field is poised to extend its reach to engineering larger more complex organs and assist in closing the gap between supply and demand[4,5].

There are many difficulties in the engineering of large complex organs of the body, with two of the most basic challenges being structure and size. An organ is comprised of at least two types of tissue functioning together for a common purpose. Therefore the successful engineering of an organ must include simultaneously engineering multiple tissues and coordinating the growth of many types of cells. In addition, it is known that cells cannot survive more than 1-3 mm from an oxygen and nutrition source [6]. Unfortunately nearly all organs (i.e. brain, liver, kidney, muscle) are thicker than 3 mm and therefore need an internal vascular supply network to ensure cell survival.

Decellularization is one technique being explored to successfully engineer functional organs [7]. This method aims to utilize nature's solution to the size and structure problem for large internal organs such as the liver. Decellularization is the removal of the cellular components of tissue while preserving the noncellular support structure, the extracellular matrix (ECM). ECM is primarily made up of various types of collagen but also includes embedded signaling proteins which are known to regulate cell differentation and growth. The decellularization process has

been shown to leave behind an intact de-endothelialized vascular tree. Once an organ has been decellularized, stem cells can be reintroduced into the scaffold and redistributed throughout the organ via the intact vascular tree and triggered to grow and differentiate into the proper cells by the signal proteins left behind in the ECM.

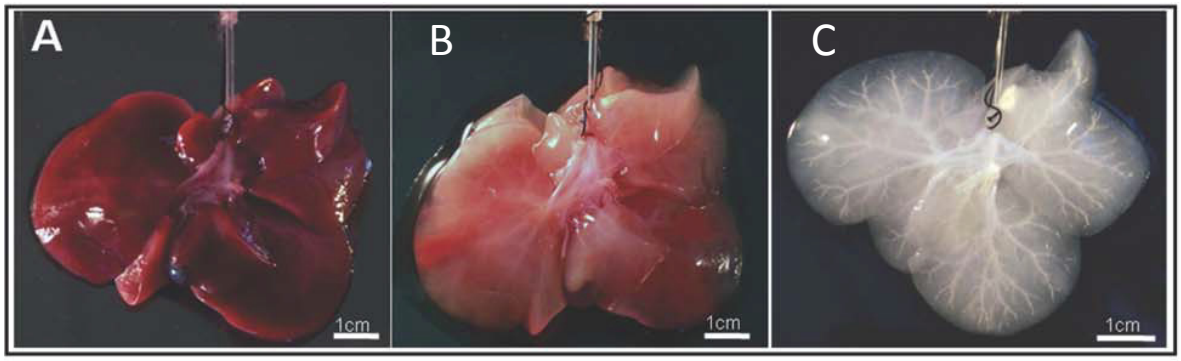

Fig 1- 1: Liver tissue during various states of decellularization: native (A), partially decellularized (B), and fully decellularized (C). [Baptista et al.]

One organ in which the decellularization technique has shown promise is the liver (Fig 1-1) [8]. The liver is the largest internal organ in the body and through highly specialized tissue is responsible for removing toxins and secreting proteins to the blood. While it may seem like an unlikely organ for experimental engineering due to its size and complexity, other aspects of the organ make it an ideal candidate. At any one time the liver can hold as much as 10-15% of the body's entire blood supply, a testament to the vascular nature of the organ [9]. The liver also has a natural regenerative ability unmatched in any other internal organ; it is able to regrow to its original size from as little as 25% of its starting mass [9].

1.2 *Mechanosensitivity*

The concept that mechanical loading affects tissue is not a new one. Wolff's law dating to 1892 states that "over time, the mechanical load applied to living bone influences the structure of the bone itself" [10]. While this cellular mechanosensitivity makes intuitive sense in load bearing tissues, the effect of the mechanical environment on cells of non-load bearing tissues may be

surprising. As early as 1952, mesenchymal cells were noted as having a "dependence of cell shape and cell movement on the physical structure of the medium" (Fig 1-2) [11,12]. The current understanding is that the phenotype of some cells is directly influenced by the stiffness of the underlying substrate on which they are anchored [13]. The primary cell type of the liver, the hepatocyte, has been shown to alter cell differentation and proliferation based on the underlying structure and mechanical properties of the ECM [14,15]. Similarly, cellular mechanosensitivity has been reported in other liver cells such as stellate cells, portal fibroblasts, and hepatic stem and progenitor cells [15,16]. The mechanosensitivity of the cells populating the liver and specifically of the stem and progenitor cells repopulating a decellularized liver scaffold highlights the importance of characterizing the biomechanical properties of the scaffold at the cellular scale.

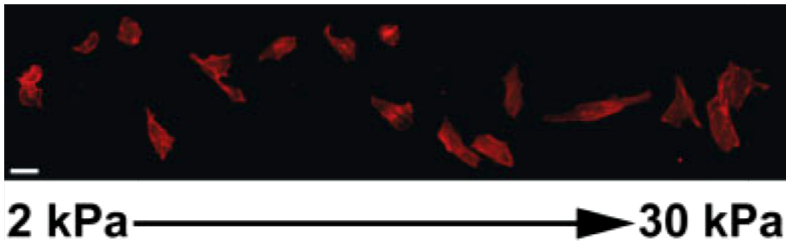

Fig 1- 2: Morphology of A7 melanoma cells on a gel with stiffness gradient increasing from 2 kPa at the left side of the image to 30 kPa at the right side of the image. [Janmey et al.]

1.3 *Structure of the Liver*

Like other biologic tissue, the liver has a hierarchial structure. On the gross level, the organ is surrounded by a fibrous capsule, and can be divided into 4 lobes, the left lobe, right lobe, quadrate lobe, and caudate lobe [9]. The liver is perfused with both an arterial and portal venous blood supply. Twenty percent of the blood supply to the liver is from the aorta and enters the liver via the hepatic artery while the remaining 80% is post-gastrointestinal and enters through the portal vein. Blood drains from the liver to the inferior vena cava by way of the hepatic veins.

On the functional level, the liver is made up of 50,000-100,000 lobules, each 0.8-2 mm in diameter [9]. The lobule is a hexagonal structure with a central vein, a branch of the hepatic vein, at its center and portal triads (branches of the hepatic artery, portal vein, and bile duct) at its nodes (Fig 1-3). Sinusoids, which are specialized leaky-walled capillaries, extend radially from the portal triads to the central vein. The sinusoids are lined by a layer of sinusoidal endothelial cells. These cells are separated from the hepatocytes by the thin 1μm-wide Space of Disse.

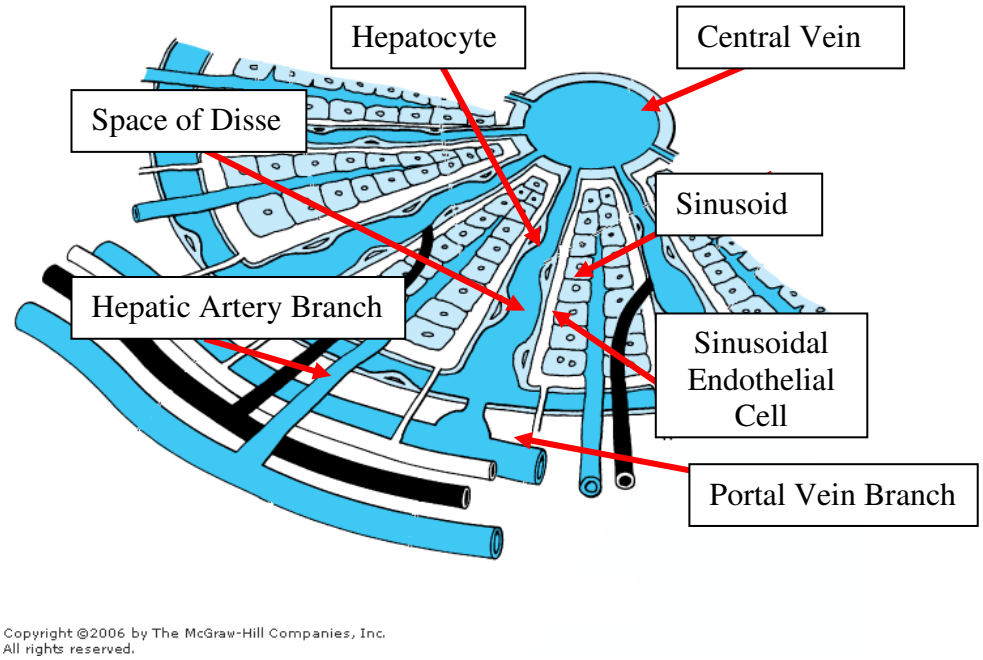

Fig 1- 3: Diagram of a liver lobule showing the hepatocytes, sinusoids, sinusoidal endothelial cells, space of Disse, central vein, hepatic artery, and portal vein.

Blood flowing into the liver from the hepatic artery and portal vein arrives at the outside of a lobule where it flows through the sinusoids on its way to the central vein and eventually to the inferior vena cava. As it passes through the sinusoid, plasma is able to leak through fenestrae (gaps in the sinusoidal wall) and into the Space of Disse. It is here in the Space of Disse that plasma and hepatocytes can interact allowing the liver to perform its necessary functions.

Underlying all of the intricate cellular components of the liver is a scaffold of ECM. The hepatic ECM is responsible for structural integrity and controlling liver cell proliferation, migration, differentiation, and gene expression [17]. Collagen forms the major structural scaffold, with types I, III, IV, and V being the most abundant found in the liver [18]. Glycoproteins, including laminin and fibronectin, and proteoglycans are additional components of the ECM that are integral in cellular interaction and tissue hydration [17]. The ECM is extremely important in liver physiology and pathology and any disruption to its normal state causes changes in liver function[19].

1.4 *Multi-Scale Material Properties*

Just as the relevant anatomy changes with length scale, the fundamental building blocks of a material and the mechanical properties which describe them change also. In the emerging field of multi-scale modeling an effort is being made to integrate the small fundamental scales with the large functional scales that exist in the hierarchial structure of biologic systems [20]. Tendon tested across the range of its hierarchial structure (tendon, collagen fibril, collagen molecule) showed a scale-dependent stress-strain response [21]. Similarly, multiscale AFM indentation testing of porcine articular cartilage found a 100 fold change in modulus with different sized tips, which is an effect not found in homogenous agarose gels [22]. This drastic modulus change was attributed to contacting many fibers in the case of the larger indenter (R=2.5 μm) and only 1 fiber with the smaller indenter (R=20nm). This finding illustrates that changes to the fundamental building blocks do not solely account for changes in mechanical properties, and that other factors such as alignment and structure also contribute. These multi-scale differences may also occur in both native and decellularized tissue and therefore mechanical testing should be performed at multiple scales.

1.5 *Indentation Testing*

As with other soft biologic materials, liver tissue can be difficult to obtain in the precise geometries needed for conventional compression or tension testing. Compounding this problem is the need to test liver tissue in its natural perfused state. Indentation testing is an alternative approach that lends itself well to testing material with irregular shape and size [23]. The method has also previously been used both in vivo and in vitro to test perfused porcine liver [24].

In its conventional form, indentation testing uses indenters with dimensions on the order of millimeters to probe the elastic-plastic response of materials such as metals and ceramics to determine hardness. This testing methodology can be utilized to test the tissue scale properties of liver using a commercial Bose Mechanical TestBench equipped with a spherical indenter. Nanoindentation, a form of indentation test, uses indenters as small as 1-20nm to probe materials while measuring the subsequent reaction force [25]. The smaller indenter allows for testing smaller formations such as those that exist in the hierarchial micro-structure of biologic tissue. The emerging field of nanoindentation has been widely used to study many types of biologic tissue ranging from rat callus [26], cartilage[27], and cortical bone[28]. This study employed both conventional indentation and nano-indentation to determine the properties of native and decellularized liver at multiple scales.

1.6 *Nano-Tissue Indenter (NTI)*

In order to perform cellular-scale testing, a novel Nano-Tissue Indenter (NTI) was developed (Fig 1-4). NTI can measure an applied force with a resolution of 283 nN and subsequent indentation with a resolution of 694 nm. The device was validated by comparing nanoindentation results of two formulations of silicone rubber with results obtained from conventional macro unconfined compression.

NTI makes use of segments of fiber optic cable as cantilevers and glass microspheres as indenters. The design allows cantilevers of varying stiffness to be used in conjuction with indenters of variable size. As a result the NTI device is a versatile instrument that can be used to test virtually any soft biologic tissue or biomaterial.

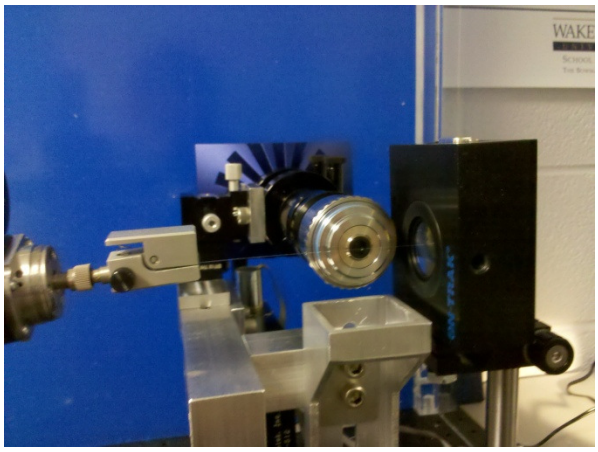

Fig 1- 4: Nano-Tissue Indenter (NTI)

1.7 *Study Objective*

The known mechanosensitivity of the cells populating the liver, and specifically of the cells repopulating a decellularized liver scaffold, highlights the importance of characterizing the biomechanical properties of the scaffold in a state relevant to cell-scaffold interactions. The vascular nature of liver tissue is evidence of the importance of fluid flow in liver biology and liver structural organization. Therefore, testing mechanical properties of decellularized and native liver in a perfused state was chosen to replicate the conditions of the recellularization process and mimic the natural in vivo environment. The goal of this work was to investigate and quantify the biomechanical properties of perfused decellularized liver scaffolds and compare them to perfused native tissue properties on both a macro and nano-scale.

1.8 *Liver Experiments and Finite Element Modeling*

Macro and nano-indentation experiments were conducted on native and decellularized liver tissue obtained from cadaveric ferrets. The livers were perfused with saline through cannulae inserted into segments of the portal vein. A Bose ElectroForce Test Bench setup was used to perform the macro- indentation-relaxation experiments on tissue perfused at 0, 3, and 6 ml/min of saline and at indentation rates of 0.01 and 1 mm/s. Nanoindentation tests were performed using NTI and tested native and decellularized tissue perfused at 6 ml/min. Additional unperfused nanoindentation tests were run on native tissue with and without the capsule. The tests were then modeled using a poroviscoelastic (PVE) finite element model to determine material parameters.

Poroviscoelasticity is a biphasic constitutive model of a material that consists of a mixture of a solid and a fluid component. In PVE, a solid inherently viscoelastic matrix is fully saturated with an inviscid incompressible fluid [29]. In addition to the viscoelastic nature of the solid, relative motion between the solid and fluid phases of the material creates an additional source of rate-dependency. PVE modeling of biological tissues stems from the study of articular cartilage and has been previously used to model other soft tissue including liver [30]. The strength of a PVE model is its ability to simultaneously predict the internal fluid and solid properties of biphasic material.

The subsequent chapters of this work including title and summary are:

Chapter 2: Nano-Indentation Device for Investigating the Biomechanics of Liver Extracellular Matrix

The aim of the first paper was to validate the concept of the NTI device and document its ability to quantify the mechanical properties of materials similar to biologic tissue.

Chapter 3: Scale-Dependent Mechanical Properties of Native and Decellularized Liver Tissue

The aim of the second study was to investigate and quantify the mechanical properties that occur in native and decellularized liver tissue at the macro and nano scales.

Chapter 4: Conclusion

The conclusion includes a summary of the overall scope of this work and a brief section containing possible future directions.

References

1. Mason C, Dunnill P (2007) A brief definition of regenerative medicine. Regenerative Medicine 3 (1):1-5. doi:10.2217/17460751.3.1.1

2. OPTN/SRTR (2009) Annual Report U.S. Organ Procurement and Transplantation Network and the Scientific Registry of Transplant Recipients: Transplant Data 1999-2008. HHS/HRSA/HSB/DOT.

3. Atala A, Bauer SB, Soker S, Yoo JJ, Retik AB Tissue-engineered autologous bladders for patients needing cystoplasty. The Lancet 367 (9518):1241-1246. doi:10.1016/s0140-6736(06)68438-9

4. Orlando G, Wood KJ, Stratta RJ, Yoo JJ, Atala A, Soker S (2011) Regenerative Medicine and Organ Transplantation: Past, Present, and Future. Transplantation 91 (12):1310-1317 1310.1097/TP.1310b1013e318219ebb318215

5. Orlando G, Baptista P, Birchall M, De Coppi P, Farney A, Guimaraes-Souza NK, Opara E, Rogers J, Seliktar D, Shapira-Schweitzer K, Stratta RJ, Atala A, Wood KJ, Soker S (2011) Regenerative medicine as applied to solid organ transplantation: current status and future challenges. Transplant International 24 (3):223-232. doi:10.1111/j.1432-2277.2010.01182.x

6. Folkman J, Hochberg M (1973) SELF-REGULATION OF GROWTH IN THREE DIMENSIONS. The Journal of Experimental Medicine 138 (4):745-753. doi:10.1084/jem.138.4.745

7. Badylak SF, Freytes DO, Gilbert TW (2009) Extracellular matrix as a biological scaffold material: Structure and function. Acta Biomaterialia 5 (1):1-13. doi:DOI: 10.1016/j.actbio.2008.09.013

8. Baptista PM, Siddiqui MM, Lozier G, Rodriguez SR, Atala A, Soker S (2011) The use of whole organ decellularization for the generation of a vascularized liver organoid. Hepatology 53 (2):604-617. doi:10.1002/hep.24067

9. Guyton AC, Hall JE (2006) Textbook of medical physiology. Elsevier Saunders, Philadelphia, Penns.

10. Ruff C, Holt B, Trinkaus E (2006) Who's afraid of the big bad Wolff?: “Wolff's law” and bone functional adaptation. American Journal of Physical Anthropology 129 (4):484-498. doi:10.1002/ajpa.20371

11. Weiss P, Garber B (1952) Shape and Movement of Mesenchyme Cells as Functions of the Physical Structure of the Medium. Proceedings of the National Academy of Sciences 38 (3):264-280

12. Janmey PA, Winer JP, Murray ME, Wen Q (2009) The hard life of soft cells. Cell Motility and the Cytoskeleton 66 (8):597-605. doi:10.1002/cm.20382

13. Discher DE, Janmey P, Wang Y-l (2005) Tissue Cells Feel and Respond to the Stiffness of Their Substrate. Science 310 (5751):1139-1143. doi:10.1126/science.1116995

14. Hansen LK, Wilhelm J, Fassett JT (2005) Regulation of Hepatocyte Cell Cycle Progression and Differentiation by Type I Collagen Structure. In: Gerald PS (ed) Current Topics in Developmental Biology, vol Volume 72. Academic Press, pp 205-236

15. Wells RG (2008) The role of matrix stiffness in regulating cell behavior. Hepatology 47 (4):1394-1400. doi:10.1002/hep.22193

16. Lozoya OA, Wauthier E, Turner RA, Barbier C, Prestwich GD, Guilak F, Superfine R, Lubkin SR, Reid LM (2011) Regulation of hepatic stem/progenitor phenotype by microenvironment stiffness in hydrogel models of the human liver stem cell niche. Biomaterials 32 (30):7389-7402. doi:10.1016/j.biomaterials.2011.06.042

17. Bedossa P, Paradis V (2003) Liver extracellular matrix in health and disease. The Journal of Pathology 200 (4):504-515. doi:10.1002/path.1397

18. Martinez-Hernandez A, Amenta PS (1993) The hepatic extracellular matrix. Virchows Archiv 423 (1):1-11. doi:10.1007/bf01606425

19. Zern MA, Reid LM (1993) Extracellular matrix: chemistry, biology, and pathobiology with emphasis on the liver. Dekker,

20. Markus J B (2011) Multiscale aspects of mechanical properties of biological materials. Journal of the Mechanical Behavior of Biomedical Materials 4 (2):125-127. doi:10.1016/j.jmbbm.2010.12.018

21. Sasaki N, Odajima S (1996) Elongation mechanism of collagen fibrils and force-strain relations of tendon at each level of structural hierarchy. Journal of Biomechanics 29 (9):1131-1136. doi:10.1016/0021-9290(96)00024-3

22. Stolz M, Raiteri R, Daniels AU, VanLandingham MR, Baschong W, Aebi U (2004) Dynamic Elastic Modulus of Porcine Articular Cartilage Determined at Two Different Levels of Tissue Organization by Indentation-Type Atomic Force Microscopy. Biophysical Journal 86 (5):3269-3283. doi:Doi: 10.1016/s0006-3495(04)74375-1

23. Ebenstein DM, Pruitt LA (2006) Nanoindentation of biological materials. Nano Today 1 (3):26-33. doi:Doi: 10.1016/s1748-0132(06)70077-9

24. Kerdok AE, Ottensmeyer MP, Howe RD (2006) Effects of perfusion on the viscoelastic characteristics of liver. Journal of Biomechanics 39 (12):2221-2231. doi:10.1016/j.jbiomech.2005.07.005

25. Fischer-Cripps AC (ed) (2002) Nanoindentation. Mechanical Engineering, 2nd edn. Springer, New York

26. Leong PL, Morgan EF (2008) Measurement of fracture callus material properties via nanoindentation. Acta Biomaterialia 4 (5):1569-1575. doi:10.1016/j.actbio.2008.02.030

27. Ferguson VL, Bushby AJ, Boyde A (2003) Nanomechanical properties and mineral concentration in articular calcified cartilage and subchondral bone. Journal of Anatomy 203 (2):191-202. doi:10.1046/j.1469-7580.2003.00193.x

28. Fan Z, Swadener JG, Rho JY, Roy ME, Pharr GM (2002) Anisotropic properties of human tibial cortical bone as measured by nanoindentation. J Orthopaed Res 20 (4):806-810. doi:10.1016/s0736-0266(01)00186-3

29. Mow VC, Kuei SC, Lai WM, Armstrong CG (1980) Biphasic Creep and Stress Relaxation of Articular Cartilage in Compression: Theory and Experiments. Journal of Biomechanical Engineering 102 (1):73-84

30. Raghunathan S, Evans D, Sparks J (2010) Poroviscoelastic Modeling of Liver Biomechanical Response in Unconfined Compression. Ann Biomed Eng 38 (5):1789-1800. doi:10.1007/s10439-010-9957-x

Chapter II

2. Nano-Indentation Device for Investigating the Biomechanics of Liver Extracellular Matrix

D.W. Evans, N.A. Vavalle, R. De Vita, P. Rajagopalan, and J.L. Sparks

The following manuscript is in review. Stylistic variations are due to the requirements of the journal. D.W. Evans built NTI, performed nano-indentation tests, and prepared the manuscript. N.A. Vavalle performed macro-unconfined compression. R. De Vita and P. Rajagopalan acted in an editorial capacity and J.S. Sparks acted in an advisory and editorial capacity.

Title

Nano-Indentation Device for Investigating the Biomechanics of Liver Extracellular Matrix

Authors

Douglas W. Evans[1,2], Nicholas A. Vavalle[1,2], Raffaella DeVita[5,2], Padma Rajagopalan[4,2], Jessica L. Sparks[1,2]

1. Department of Biomedical Engineering, Wake Forest University School of Medicine,
2. Virgina Tech – Wake Forest University School of Biomedical Engineering and Sciences
3. Department of Chemical Engineering, Virginia Polytechnic Institute and State University
4. Department of Engineering Science and Mechanics, Virginia Polytechnic Institute and State University

***Correspondence to:**

Jessica L. Sparks, Ph.D.
Department of Biomedical Engineering
Wake Forest University School of Medicine
Medical Center Blvd.
Winston Salem, NC 27157
Email: jsparks@wfubmc.edu
Phone: 336-716-4543
Fax: 336-716-5491

Abstract

Indentation testing has long been used to measure the mechanical properties of a wide range of materials from metals and ceramics to brain tissue and hydrogels. The purpose of this study was to build and validate a Nano-Tissue Indenter (NTI) capable of performing indentation testing on micro-scale structures within the liver's extracellular matrix. Two silicone-based tissue simulant materials were selected with elastic properties similar to hydrogels used for liver cell cultures. Samples of each material formulation, EcoFlex0030 (EF30) and EcoFlex0010 (EF10), were indented with NTI and also tested in unconfined compression to provide benchmark shear moduli. The resulting force and displacement measurements from NTI with resolutions of 300 nN and 700 nm respectively were analyzed using the Pietrement-Troyon model of adhesive contact. Using this method, NTI was able to distinguish a 10 kPa difference in shear modulus between EF30 and EF10 with comparable significance as unconfined compression ($p<0.001$). General agreement between the results of the two test methods is evidenced by the overlapping of the mean ± S.D. range for the NTI-indentation and benchmark unconfined compression shear moduli measured for both formulations. NTI was used successfully to perform nano-indentation tests on samples of compliant material undergoing adhesive contact, similar to the extracellular matrix of organs such as the liver.

Key Words: Spherical Indentation, Adhesive Contact, Nano-indentation, Liver Biomechanics

2.1 *Introduction*

One method to investigate the properties of a material is to use an indenter of known geometry to probe its surface. Indentation testing has long been used to measure the mechanical properties of a wide range of materials from metals and ceramics to brain tissue and hydrogels [1-5]. The method lends itself well to testing materials with irregular shape and size features that can be a barrier to conventional compression and tensile testing regimes [6]. This is particularly important in the fields of biomechanics and regenerative medicine, where specimen geometries can be problematic. Materials such as biological tissues, tissue scaffolds, and cell substrates can be difficult to obtain in precise geometries and difficult to test using conventional techniques [7-10].

The success of indentation testing on biological tissue and other inhomogeneous materials has led to the emergence of the field of nano-indentation, also known as instrumented indentation [11]. Nano-indentation typically detects displacements from 1 nm-20 μm and forces from 10 pN -500 mN [12,13]. While conventional macro-indentation uses indenters with dimensions on the order of millimeters [6], nano-indentation uses indenters as small as 10 nm and as large as 1000 μm [9,14]. The smaller probe allows for testing smaller samples including structures that exist within the hierarchial composition of biological tissue. The technique has been used to characterize rat callus [15], cartilage [16] , cortical bone [17], and hydrogels [18] using a variety of commercially available and custom designed devices.

Many commercially available nano-indentation devices utilize electromagnetic or electrostatic actuation of force and a capacitive sensor to measure displacement [19-23]. As a result, these devices are force-controlled and, when equipped with a feedback loop, are suited for studying time-dependent material properties [11]. Such designs are appropriate for studying viscoelasticity; however, difficulty in accurately detecting the surface of a compliant material can lead to significant errors [24]. One way to overcome this surface detection problem is to begin a

test with the indenter above a sample, easily accomplished in a device with displacement-control [9]. Displacement-controlled devices such as atomic force microscopes (AFMs) and other custom scanning probe microscopes operate using cantilevers of known stiffness to prod samples as the cantilever deflection is monitored by a laser [25]. Commercial AFMs utilize expensive silicon-nitride cantilevers with tip radii on the order of 5-10 nm which are normally created for imaging purposes and frequently suffer from imprecise geometry [12]. Another limitation of commercial AFM is the limited vertical sample dimension that the device can accommodate due to limited z-axis range [26].

The objective of this study was to design and build an instrumented indentation device that would enable us to investigate the mechanical properties of the matrix micro-architecture of the liver. Since several cell populations in the liver exhibit mechanosensitivity [27], it is important to understand and quantify the biomechanical properties of liver matrix at a scale relevant for cellular perception. [28]. Hepatocytes range from 15-25 μm in diameter [29,30], setting the scale of interest in the upper end of the nano-indentation spectrum. As with other biological materials, liver tissue is extremely compliant [31]. For this reason, a displacement controlled nano-indentation device design was selected, suitable for testing compliant materials in which adhesion forces between the indenter and sample may be significant [9]. The design incorporates fiberoptic cantilevers which provide the ability to vary cantilever stiffness and indenter shape and size at an economical cost.

This paper reports the successful development of the device and the results of experiments designed to evaluate device performance. Specifically, the device components, calibration methods, operating techniques, and cantilever stiffness characterization are described in detail. In addition, a mathematical model is identified that is appropriate for calculating the elastic modulus of compliant materials tested in nano-indentation. Implementation of the device is then illustrated in nano-indentation tests of two silicone rubber materials with elastic moduli similar to the range

reported for hydrogel used to culture hepatocytes [32], and the results are compared with traditional macroscopic unconfined compression experiments of the same materials. Finally, an uncertainty analysis is provided in order to determine the resolution of force and displacement measurements obtained using the device.

2.2 *Materials and Methods*

2.2.1 Device Overview

The device reported in this study, termed the Nano-Tissue Indenter (NTI), was inspired by a previously developed embryonic tissue testing apparatus [33]. NTI utilizes a segment of fiber-optic cable as a cantilever that deflects upward as a sample is raised into contact with an attached spherical indenter (Fig 2-1). Cantilever deflection, which is proportional to applied force, is monitored using an optical position detector. At the same time a horizontally positioned camera captures video of the contact which is later analyzed to provide a direct measurement of indentation depth. The device is constructed on an optical breadboard with an acrylic enclosure to isolate the instrument from air currents.

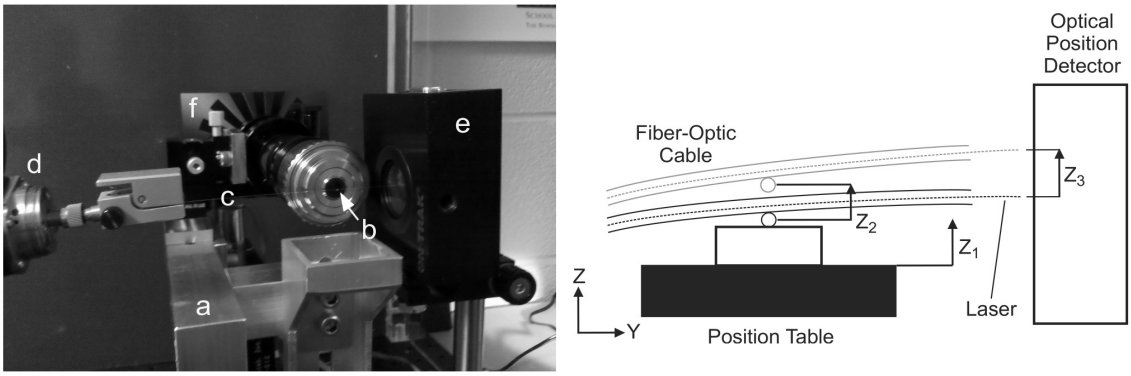

Fig 2- 1 (Left) Picture of NTI showing components (a) 3-axis translation table, (b) glass microsphere indenter (c) fiber-optic cantilever (d) laser with focusing fiberport (e) position detector (f) microscope objective with attached video camera. (Right) Schematic of the side view of NTI showing the positioning and displacement of the position table (Z1), microsphere indenter (Z2), and position detector (Z3)

2.2.2 Components

Position Table

Sample position is controlled using a custom 3-axis translation table (USEuro-Tek) with 3 DC servo motors and fine pitched screws to achieve 355 nm resolution in the X and Y directions and 102 nm resolution in the Z direction (Fig 2-1 a). Maximum axis-velocity can be set anywhere between .001 – 10 mm/s.

Glass Microsphere Indenter and Fiber-Optic Cantilever

A glass microsphere (Cosphereic) with diameter ranging from 20 μm to 60 μm is used as a rigid indenter to probe a sample material (Fig 2-1 b). The microsphere is attached via a small bead of epoxy (Loctite Instant Mix 5 minutes) to a segment of fiber-optic cable (AFS-105/125 Thor Labs) stripped of its outer protective plastic coating (Fig 2-1 c). Cantilever stiffness can be controlled by varying the effective length of the cable (L_{eff}), which is the location of the microsphere indenter from the fixed end of the cable. L_{eff} can range from 20 mm to 80 mm and results in effective cantilever stiffnesses (K_{eff}) of 0.4 - 0.004 N/m.

Laser

A laser diode module (Newport Corporation) emits 30 mW of infrared energy at a wave length of 830 nm in a 1 mm circular diameter beam. A fiberport (Thor labs) with 6 degrees of micropositioning secures the cantilever in position, and a bare fiber adapter (Newport Corporation) focuses the laser (Fig 2-1 d).

Position Detector

A PSM2-10 position sensor module and OT-301 signal amplifier (On-Trak Photonics) are used to accurately determine the location of the laser beam (Fig 2-1 e). The PSM2-10 is capable of detecting light on a 1 cm^2 sensor and calculating the centroid with a resolution of 250 nm. Before the laser beam contacts the detector, it passes through 2 filters. The first filter is a neutral density (Newport Corporation) filter with an optical density of 2 to attenuate the beam. The second is a

bandpass filter (Newport Corporation) to minimize the effects of ambient light. The signal amplifier outputs an analog signal for Y and Z positions of the centroid. A USB-6009 14-bit data acquisition unit (National Instruments) then samples the analog signals.

Microscope Objective and Video Camera

A LD-Plan Neofluar 40x objective (Zeiss) with long working distance and an AxioCam MRc (Zeiss) are connected using an Infini-tube-Z optical tube (10x, Infinity Inc) (Fig 2-1 f). Using a second computer dedicated to imaging, AxioVision LE (4.8.1 Zeiss) provides a live video of the indentation tests. The objective and camera are mounted directly to the position table to move with the sample. A three-axis manual micro-positioner (Thor Labs) allows objective and camera to move relative to the sample to allow for focusing and alignment.

2.2.3 Cantilever Stiffness and Position Detector Calibration

Before performing indentation tests with NTI it is necessary to first determine two quantities. The first is the effective stiffness of the fiber-optic cantilever (K_{eff}) and the second is the relationship between the displacement of the microsphere indenter and the output of the position detector (calibration constant *A*). Effective stiffness for a particular cantilever is determined by hanging wire weights (4.23 -10.01 mg) at the location of the attached microsphere indenter and recording the subsequent vertical displacements using the camera. K_{eff} is then calculated as the slope of a linear regression fit to the force-displacement data.

Position detector calibration consists of determining the relationship between the displacement of the indenter (Z_2) and the displacement monitored by the position detector (Z_3). Z_2 and Z_3 are related through a proportionality constant, *A*. The calibration constant is determined by performing a control indentation test on a sufficiently rigid material so that no indentation occurs (Z_1=Z_2 in Fig 2-1), such as a piece of metal. After contact is made between the metal sample and the indenter, the position table is raised moving the tip of the fiber-optic cantilever across the position detector's range. Linear regression is used to fit a linear relationship to the position of

the indenter (Z_2) and the output of the position detector (Z_3) with the slope defined as the calibration constant *A*.

2.2.4 Operating NTI

Indentation tests are performed by first aligning a sample to be tested on the position table directly under the microsphere indenter. The manual 3-axis micro-positioner attached to the camera is then adjusted so that the plane of focus is behind the front edge of the sample. The position table is then moved in the x-direction (as defined in Fig 2-1) until the indenter comes into focus above the top surface of the sample.

NTI is powered by two computers, one running a custom Labview interface (National Instruments) and a second dedicated to gathering video data and performing image analysis (Fig 2-2). The Labview interface simultaneously controls the position table and the data acquired from the position detector. The program was designed to trigger the screen capture program Camtasia (TechSmith Corp), running on the second computer at the start and stop of data acquisition. The output measurement file from Labview is then combined with the imaging tracking data using custom Matlab code (Mathworks).

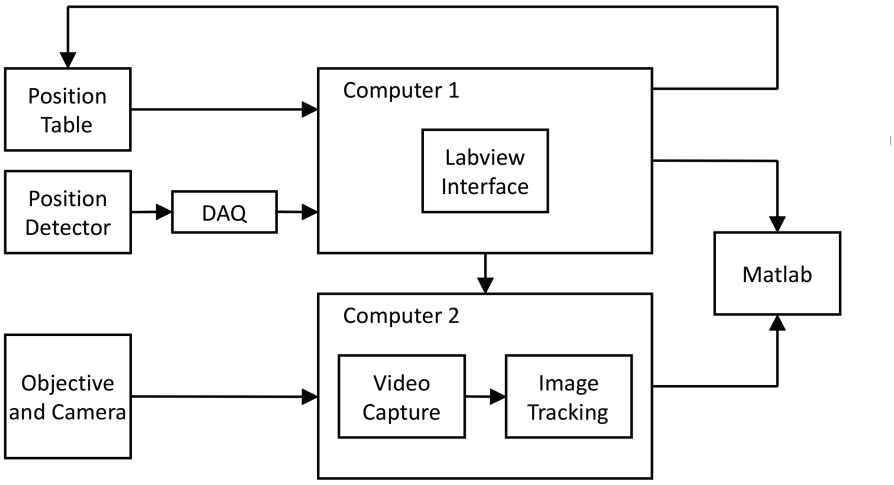

Fig 2- 2 Flow of data from NTI components through hardware and into software

After starting data acquisition, the position table is raised at a constant velocity for 15 mm and then lowered at the same velocity until 'pull-off', when the indenter loses contact with the sample. Starting the indentation test before contact is made between the sample and the indenter and ending the test after they separate ensures that all necessary data for the test have been recorded.

Following the indentation test an image tracking program, Tracker v3.10 (Open Source Physics), is used to track the relative position of the indenter in the field of view of the camera. By specifying a cluster of pixels at the center of the indenter, an autotracking function allows the program to automatically track the cluster of pixels throughout the video. Starting with the first image, the indenter moves downwards through the frame until contact is made between the sample and the indenter. At this point, any displacement of the indenter relative to the camera frame is equal to the indentation that has occurred, (Z_1-Z_2). Tracking ends once contact is lost at 'pull-off', the point when the indenter quickly returns to its equilibrium position and is absent from the image.

The position detector data is converted into force data using Eqn 1:

$$F_n = K_{eff} A Z_3 \qquad (1)$$

where K_{eff} is the stiffness of the cantilever, A is the calibration constant and Z_3 is the output from the detector. Image tracking data in the form of pixel positions are converted into distance using Eqn 2:

$$\delta = Z_2 B = \frac{Z_2 S_m}{X} \qquad (2)$$

where Z_2 is pixel position tracked by the software and B is distance per pixel determined using a scale micrometer (Fisher Scientific) in the field of view of the camera (X is the number of pixels

between the micrometer's divisions of length S_m). The two data sets are plotted forming a force vs displacement curve similar to Fig 2-3b.

2.3 *Mathematical Model*

The simplest theory to model indentation, Hertzian contact mechanics, is valid for small strains within the elastic limit of a material and assumes frictionless contact [34]. However, when dealing with soft materials such as rubber and biological tissue or when contact is on the micro- and nano-scales, adhesive forces such as Van der Waals forces between the indenter and the sample begin to play a significant role in material behavior [35]. Hertzian contact has been modified to account for adhesion based on surface energy in the Johnson-Kendall-Roberts (JKR) model, Eqn 3 & 4:

$$a_{(JKR)} = \left[\frac{3R}{4E_r} \left(\sqrt{F_{ad(JKR)}} + \sqrt{F_n + F_{ad(JKR)}} \right)^2 \right]^{1/3} \tag{3}$$

$$\delta_{JKR} = \frac{a^2_{(JKR)}}{R} - \sqrt{\frac{4a_{(JKR)}F_{ad(JRK)}}{3RE_r}} \tag{4}$$

and based on cohesive forces outside the contact area in the Derjaguin-Muller-Toporov (DMT) model, Eqn 5 & 6: [36,37].

$$a_{(DMT)} = \left[\frac{3R}{4E_r} \left(F_n + F_{ad(DMT)} \right) \right]^{1/3} \tag{5}$$

$$\delta_{(DMT)} = \frac{a^2_{(DMT)}}{R} \tag{6}$$

The JKR and DMT equations use the distances defined in Fig 2-3(a) and the forces shown in Fig 2-3(b), where R is the radius of the indenter, a is the radius of the contact area, δ is the displacement of the indenter, F_n is the applied force and F_{ad} is the maximum adhesive force.

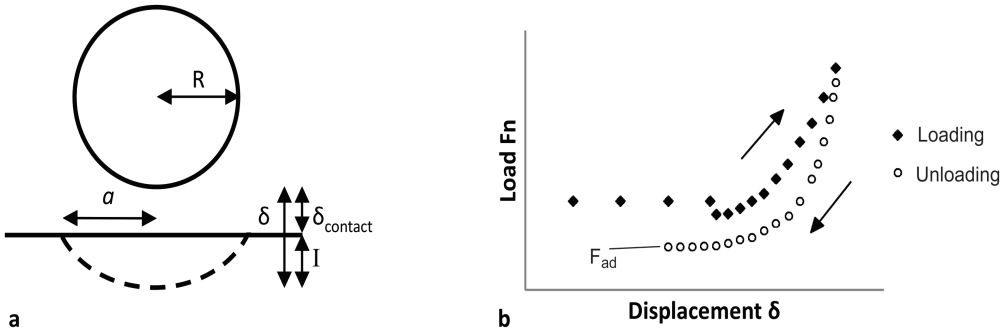

Fig 2- 3 (a) Important distances in spherical indentation relevant to models (b) Typical load displacement data for an adhesive spherical indentation test

The JKR and DMT models have been shown to represent the opposing extremes of adhesive contact with JKR excelling for strong adhesive contact using large indenters and DMT prevailing for weak adhesive contact using small indenters [38]. In order to bridge the gap, a dimensionless Tabor parameter:

$$\mu = \left(\frac{R\Delta\gamma^2}{z_0^3 E_r} \right)^{1/3} \tag{7}$$

has been defined to determine which model suits a particular indentation, where $\Delta\gamma$ is the work of adhesion, R is radius of the indentor, and z_0 is the equilibrium separation of surfaces [39]. E_r is the reduced modulus:

$$\frac{1}{E_r} = \frac{1-v_i^2}{E_i} + \frac{1-v_s^2}{E_s} \tag{8}$$

with v as Poisson's ratio, E as Young's modulus and the subscripts i and s refer to the indenter and the sample.

When $\mu < .1$ the DMT model applies and when $\mu > 5$ JKR theory dominates. For contacts that fall in between the two models ($.1 \leq \mu \leq 5$) the analytical Maugis-Dugdale solution describes the interaction between indenter and surface[40]. Pietremont and Troyon developed generalized

equations (PT model) that closely approximates the Maugis-Dugdale solution for fitting elastic indentation depth versus load data [38].

$$I = \delta - \delta_{contact} = \frac{a_0^2}{R}\left[\left(\frac{\alpha + \sqrt{1 + F_n/F_{ad}}}{1+\alpha}\right)^{\frac{4}{3}} - S_{(\alpha)}\left(\frac{\alpha + \sqrt{1 + F_n/F_{ad}}}{1+\alpha}\right)^{\frac{2}{3}\beta_{(\alpha)}}\right] \quad (9)$$

$$S_{(\alpha)} = -2.160\alpha^{0.019} + 2.7531\alpha^{0.064} + 0.073\alpha^{1.919} \quad (10)$$

$$\beta_{(\alpha)} = 0.516\alpha^4 - 0.683\alpha^3 + 0.253\alpha^2 + 0.429\alpha \quad (11)$$

Equation 9 has been slightly modified by adding an extra displacement variable ($\delta_{contact}$) similar to a modification proposed by Ebenstein and Wahl for a simplified JKR fitting procedure[41].

In this work, the PT equations are used to fit free parameters α, $\delta_{contact}$, and a_0 (the contact radius at zero applied load) to experimental load (F_n) and displacement (δ) data. The maximum adhesive force (F_{ad}) can be determined directly from experimental data from the last force measurement occuring before 'pull-off'. The parameters of $S(\alpha)$ and $\beta(\alpha)$ (Eqn 10 and 11), depend directly on the value of α which can vary from 0 to 1 and is similar to the Tabor coefficient. When α=0, $S(\alpha)$=0 and $\beta(\alpha)$=0 and Eqn 9 reduces to the DMT model. When α=1, $S(\alpha)$=2/3 and $\beta(\alpha)$=1/2 and Eqn 7 reduces to the JKR model.

The parameter α is used to calculate the non-dimensional parameters $\overline{a_{0(\alpha)}}$ and $\overline{F_{ad(\alpha)}}$ found by Pietrement and Troyon to approximate the Maguis-Dugdale solution.

$$\overline{a_{o(\alpha)}} = -0.451\alpha^4 + 1.417\alpha^3 - 1.365\alpha^2 + 0.950\alpha + 1.264 \quad (12)$$

$$\overline{F_{ad(\alpha)}} = 0.267\alpha^2 - 0.767\alpha + 2.00 \quad (13)$$

Once α, a_0, and $\delta_{contact}$ have been found using a least-squares algorithm and the non-dimensional parameters have been calculated using Eqn 12 and 13, measured values of R and F_{ad} are combined to determine the reduced modulus.

$$E_r = \frac{3}{4}\left(\frac{\overline{a_{0(\alpha)}}}{a_0}\right)^3\left(\frac{F_{ad}}{\overline{F_{ad(\alpha)}}}\right)R \tag{14}$$

Assuming the glass microsphere to be rigid, Young's modulus for a compliant sample material is calculated using Eqn 15.

$$E_s = \frac{3(1-v_s^2)RF_{ad}\overline{a_{0(\alpha)}}^3}{4\overline{F_{ad(\alpha)}}a_0^3} \tag{15}$$

2.4 *Validation*

Two formulations of silicone rubber, EcoFlex0030 (EF30) and EcoFlex0010 (EF10) were tested in both macroscopic unconfined compression (UC) and nano-indentation (NI). Results from UC were used to calculate the mean shear modulus of each material, to serve as a benchmark for comparison with NTI-based NI measurements on the same materials.

2.4.1 Macroscopic Unconfined Compression

Prior to testing with the NTI device, six samples of each silicone rubber were tested in traditional unconfined compression using a mechanical testing system (Bose-Electroforce LM1 TestBench). Samples were cylindrical in shape with a nominal diameter of 36mm and height of 24mm. Unconfined uniaxial compression experiments to 25% strain were performed on EF30 and EF10 resulting in stress-stretch ratio curves for each formulation. The UC used platens lubricated with petroleum jelly to prevent barreling and approximate a frictionless boundary condition.

A one-term Ogden model for an incompressible, isotropic, hyperelastic solid was used to model the results from each UC experiment:

$$\phi = \frac{2G}{\rho^2}\left(\bar{\lambda}_1^{\rho} + \bar{\lambda}_2^{\rho} + \bar{\lambda}_3^{\rho} - 3\right) \tag{16}$$

with φ as the strain energy density per undeformed unit volume, G as the shear modulus, ρ as the strain hardening exponent, and λ_1, λ_2, λ_3 as the principal stretch ratios[42].

Under plane stress of uniaxial compression or extension, Eqn 16 reduces to the expression for stress in the loading direction:

$$\sigma_z = \frac{2G}{\rho}\left[\lambda_z^{\rho-1} - \lambda_z^{-1-\frac{\rho}{2}}\right] \tag{17}$$

where σ_z is the engineering stress along the loading axis and λ_z is the stretch ratio along the loading axis [43]. A least-squares fit was used to find values of G and ρ.

2.4.2 Nano-Indentation with NTI

Following the unconfined compression experiments, each sample was tested under nano-indentation using the NTI. The tests were performed at a maximum nominal table velocity of 10 μm/s and consisted of raising the position table 1500 μm and lowering the table until indenter pull-off. All indentation tests utilized the same fiber-optic cantilever (L_{eff}= 60.33 mm) and microsphere indenter (R= 28 μm). Prior to the indentations, cantilever stiffness characterization and position detector calibration were performed to determine K_{eff} and A. The PT equations were fit to the resulting force-displacement data and each sample's elastic modulus was found using Eqn 15. Elastic modulus was then transformed into an equivalent shear modulus using Eqn 18 assuming silicone to be incompressible.

$$G = \frac{E}{2(1+v_s)} \tag{18}$$

The transformation allows for a direct comparison to be made between the shear modulus obtained through nano-indentation and unconfined compression.

2.4.3 Statistical Methods

The shear moduli obtained for each silicone sample tested in UC and NI were averaged, resulting in two mean moduli values for each formulation ($G_{UC\text{-}EF30}$, $G_{UC\text{-}EF10}$, $G_{NI\text{-}EF30}$, and $G_{NI\text{-}EF10}$). Student's T-tests were used to determine if statistical differences exist between mean values from each formulation across testing regimes ($G_{UC\text{-}EF30}$ with $G_{NI\text{-}EF30}$ and $G_{UC\text{-}EF10}$ with $G_{NI\text{-}EF10}$) at a significance level of 0.01.

2.5 *Results*

2.5.1 Stiffness vs Effective Length

The effective stiffness of each fiber-optic cantilever depends on the location of the microsphere indenter from the fixed end of cable. This distance, defined as effective length (L_{eff}) is crucial to the results of each indentation test, as a cable too stiff will lead to insufficent bending to determine force and a cable too compliant will lead to insufficent indentation to determine a Young's modulus. To properly place the indentor, the stiffness of a stripped AFS-105/125 cable was characterized as a function of L_{eff}. Figure 2-4a shows the results from hanging weights (4.23 -10.01 mg) at different positions and the least-squares linear regression line for each position ($0.9653 \leq R^2 \leq 0.9987$). Figure 2-4b depicts the stiffness obtained from the slope of each regression line against L_{eff}, as well as a least squares regression power curve fit to the data (R^2=0.9920).

$$K = 8.4505 \cdot 10^{-7} L_{eff}^{-3.3448} \qquad (19)$$

This equation is useful for estimating where to place a microsphere indenter to achieve a cantilever with a desired stiffness (units of K is N/m and L_{eff} is m).

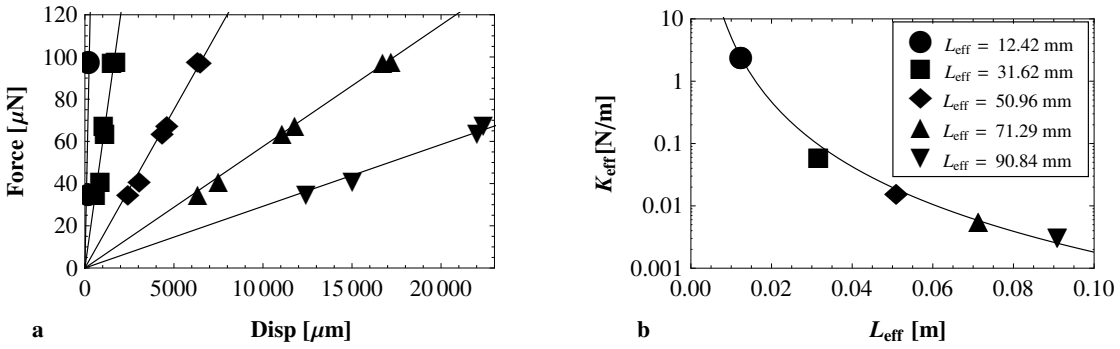

Fig 2- 4 (a) Force-deflection data obtained from hanging weights at various positions (various values for L_{eff}) on a stripped AFS-105/125 fiber-optic cable (b) Stiffness verse length of the stripped AFS-105/125 fiber-optic cable and fitted power curve (Eqn 19) (R^2=0.9920)

2.5.2 Cantilever Stiffness Characterization

The cable created and used for the nano-indentation tests had a microsphere with radius R=28 μm and located 60.33 mm from the fixed point of the cable (L_{eff}=60.33 mm). The linear regression on the force-displacement data obtained through optical measurements of vertical displacement from wire weights (n=20) (Fig 2-5) resulted in an effective stiffness of 0.0104 N/m (R^2=0.9988), similar to the stiffness predicted by Eqn 19 of 0.0101 N/m.

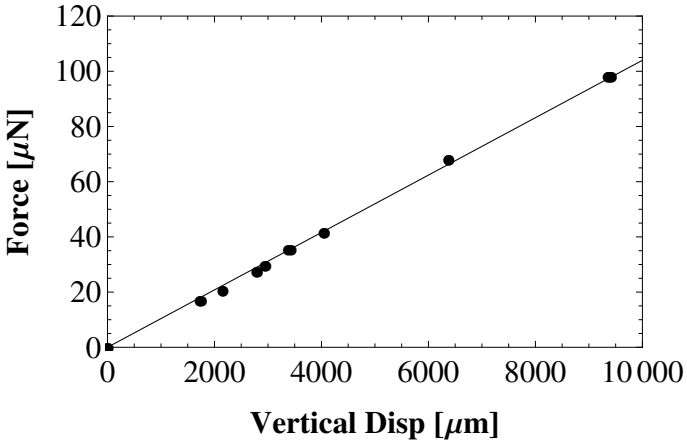

Fig 2- 5 Force-displacement data (n=20) for the cantilever used in all 11 silicone experiments. Linear regression provides a stiffness value of 0.0104 N/m (R^2=0.9988)

2.5.3 Position Detector Calibration Results

Fig 2-6 shows the results from the control indentation test performed to determine the calibration constant, *A*, which defines the relationship between the displacement of the indenter and the change in position detector voltage. These tests used the same cantilever and cantilever-position detector alignment as the EcoFlex indentation experiments reported in the following nano-indentation results section.

In Fig 2-6, the voltage recorded from the position detector is shown on the same time scale as table position and indenter position tracked from video of the test. At time (a), the table begins traveling upwards and in the video the indenter is seen moving downwards through the frame until contact is made with the sample at time (b). After contact, the indenter travels upward with the position table with no indentation taking place until the table reaches target position. At time (d) the table reverses its course, lowering the indenter below the initial contact position due to adhesion between the indenter and the sample. When the maximum adhesion force (F_{ad}) has been matched by the deformation of the cantilever, the indenter pulls-off and the sample returns to its equilibrium position out of frame on the video (e).

From this data set, the relationship between the displacement of the indenter and the change in position detector voltage was found to be highly linear within the operating range of the device (Fig 2-7). *A* is calculated as $\Delta\delta_{PD}/\Delta V$, the slope of the table position data and detector voltage over the duration of contact. Linear regression determined *A* for this cantilever-position detector alignment to be 284.89 μm/V (R^2=0.9998).

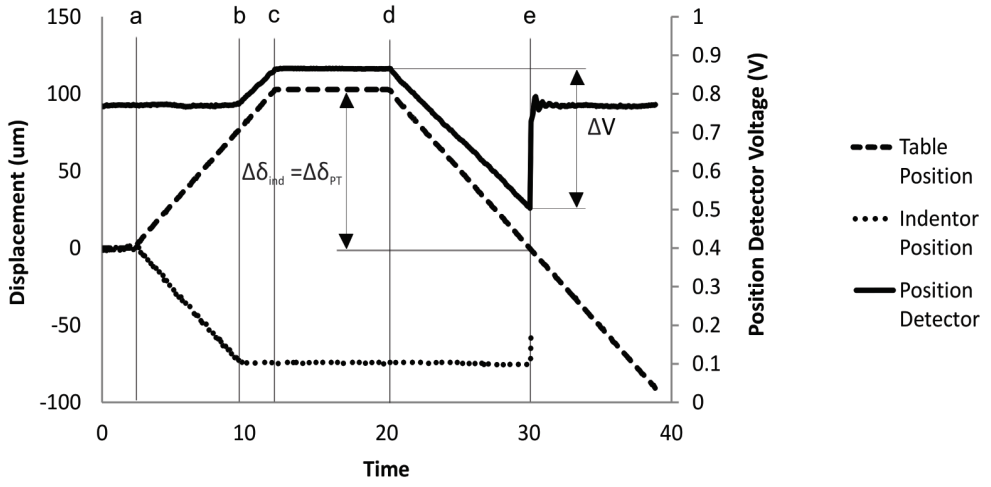

Fig 2- 6 Typical data from a control test with no indentation on a metal sample, where time point (a) marks the start of table motion, (b) contact between sample and indenter, (c) table reaching maximum position, (d) start of table lowering, and (e) 'pull off' loss of contact between indenter and sample

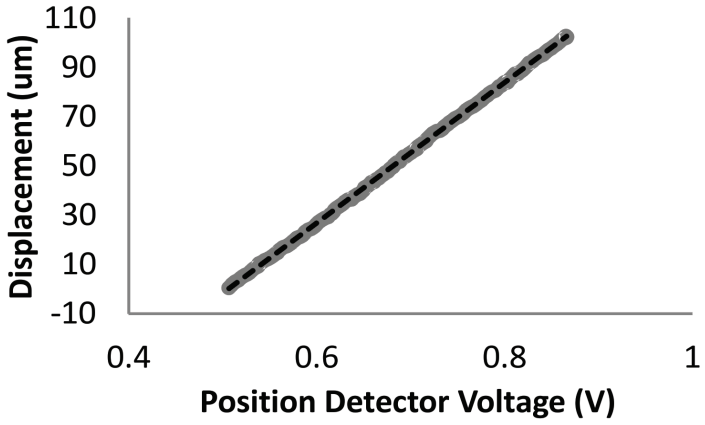

Fig 2- 7 The graph of position table displacement vs. position detector voltage spanning the time period between points (d) and (e) in Fig 2-6. The least-squares regression line with slope A=284.89 μm/V (R^2=.9998) relates the motion of the microsphere indenter to the voltage tracked by the position detector

2.5.4 Nano-Indentation Results

Representative results from the silicone NI tests are shown in Fig 2-8. In the figure, the position detector voltage output has been transformed to force output using K_{eff} and A with Eqn 1. The indenter position data has been magnified by a factor of 10 to show the change in indenter position after contact has been made. Time point (a) represents contact between the indenter and sample, point (b) is the maximum height of the table and the division between the loading and unloading portions of the test, and point (c) marks pull-off and the end point of data from video tracking.

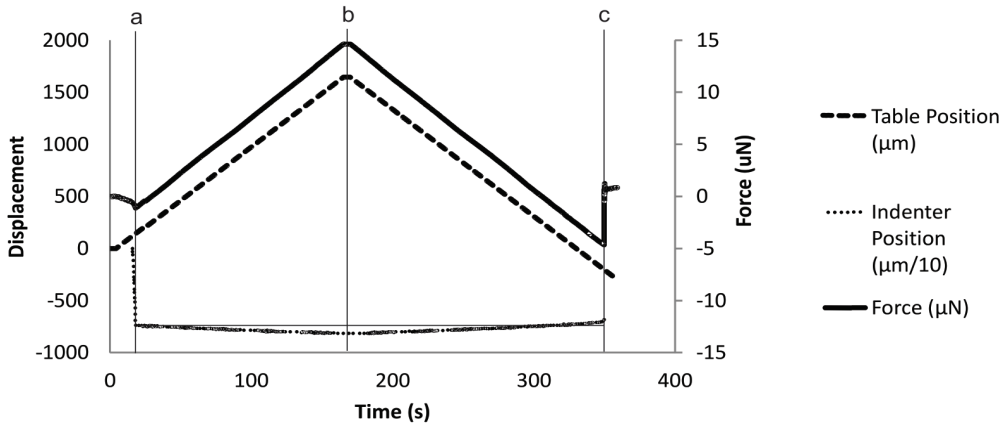

Fig 2- 8 Typical data from an indentation test with indenter position magnified by 10 to show indentation. (a) marks contact between indenter and sample, (b) maximum table position, force, and maximum indentation, and (c) marks 'pull-off'

Force verse indenter displacement during the unloading portion, extracted from Fig 2-8, is plotted in Fig 2-9. Also shown on Fig 2-9 is the PT model (Eqn 9) fit to the experimental data. Data analysis is focused on the unloading curve because it is the portion of data that sheds light on adhesion. An adhesive force during contact causes the unloading curve in Fig 2-9 to extend into negative displacements at negative force. As the sample is being unloaded, the adhesive force pulls the sample above the location of initial contact. This negative indentation is seen until the tensile force from the cantilever exceeds the maximum adhesive force marked as the minimum

force in the data sets. At this point the indenter pulls-off the sample and the corresponding force F_{ad} is used in the optimization of Eqn 2-9.

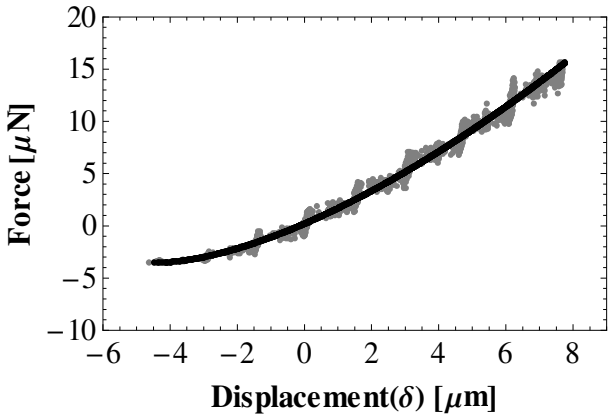

Fig 2- 9 Typical force-displacement data from the unloading portion of an indentation test of silicon rubber and the PT model curve for the data. No hysteresis can be seen between loading and unloading dataUnconfined Compression vs Nano-Indentation

The curve fits for UC resulted in benchmark values of the average shear moduli of $G_{UC\text{-}EF30}$=22.45 ± 3.36 kPa and $G_{UC\text{-}EF10}$=12.45 ± 1.43 kPa with time constants of $\rho_{UC\text{-}EF30}$=1.52 ± 0.70 and $\rho_{UC\text{-}EF10}$=3.99 ± 0.59. Fig 2-10 shows the average stress-strain data for each formulation plotted with the average Ogden models for each formulation.

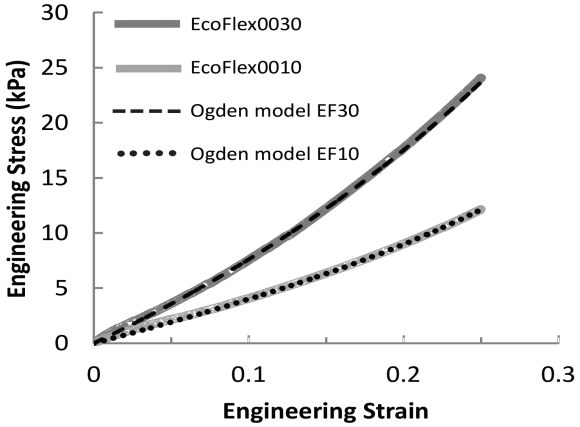

Fig 2- 10 Average stress-strain data for each silicon formulation and the one-term Ogden model for each

NI performed with NTI on 6 samples of EF30 and 5 samples of EF10 resulted in force displacement curves that were fit using the PT equations (Eqn 9-14) (Fig 2-11). Young's modulus was calculated for each test using Eqn 15 and transformed into an equivalent shear modulus using Eqn 18, assuming the silicone to be incompressible (ν=.5). The analysis resulted in mean shear modulus values of $G_{NI\text{-}EF30}$=19.43 ± 2.33 kPa and $G_{NI\text{-}EF10}$=9.84 ± 1.89 kPa.

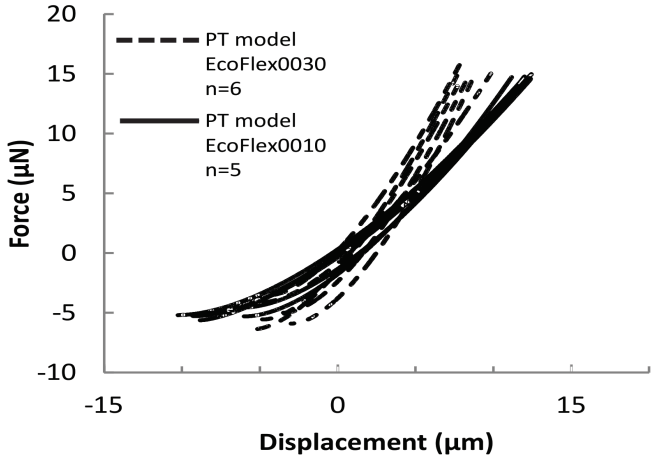

Fig 2- 11 Optimized PT models for each nano-indentation test performed using NTI displayed on a force-displacement graph. The dashed lines represent the samples of EF30 with average shear modulus of 19.43 ± 2.33 kPa and solid lines representing EF10 with average sample modulus of 9.84 ± 1.89 kPa

The mean shear moduli obtained from both types of tests are compared in Fig 2-12. The UC and NTI-based NI test methods both yielded similar modulus values per material formulation. In addition, both test methods were able to detect the relatively small difference (~10 kPa) between the shear mean moduli of the two silicone rubber formulations ($p<0.01$).

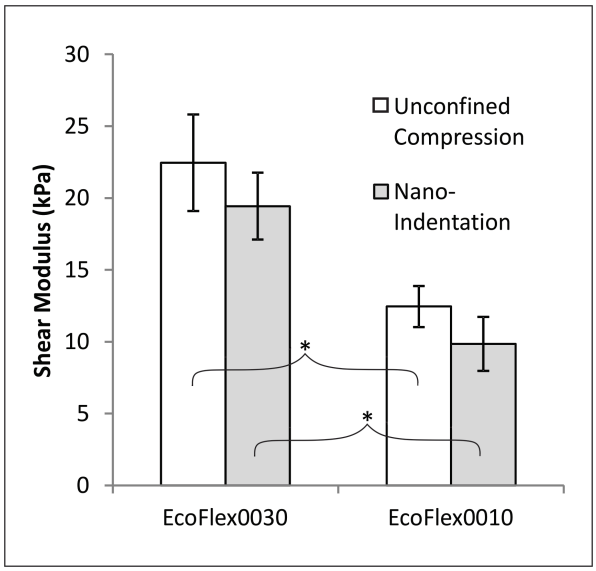

Fig 2- 12 The average shear modulus from the unconfined compression and the nano-indentation tests showing standard deviation error bars. A significant difference ($p<0.001$) was seen between the moduli values of each formulation in both testing methods

2.5.5 Uncertainty Analysis

Following the experiments, an uncertainty analysis was conducted to determine the uncertainty associated with the force and indenter displacement measurements used to find a material modulus. Using the Kline-Mclintock method Eqn 20 & 21:

$$\xi = f(\beta_1, \beta_2, ..., \beta_n) \tag{20}$$

$$\Delta\xi = \sqrt{\sum_{i=1}^{n}\left(\frac{\partial\xi}{\partial\beta_i}\Delta\beta_i\right)^2} \tag{21}$$

a value ξ has the uncertainty of $\Delta\xi$ calculated from the independent variables β_i and their uncertainties $\Delta\beta_i$ [44].

Force is calculated using Eqn 1 and depends on the stiffness of the cantilever (K_{eff}) and the calibration constant (A) determined by the control indentation and the output of the position

detector (Z_3). Indenter displacement is calculated using Eqn 2 and depends on the pixel identified by the tracking program (Z_2) and distance/pixel resolution ($B = S_m/X$) measured using a stage micrometer (Fisher Scientific). Applying Kline-McClintock to these relationships resulted in the following expressions for the uncertainty of F and δ.

$$\Delta F_n = \sqrt{\left(AZ_3\Delta K_{eff}\right)^2 + \left(K_{eff}Z_3\Delta A\right)^2 + \left(K_{eff}A\Delta Z_3\right)^2} \qquad (22)$$

$$\Delta\delta = \sqrt{\left(\frac{S_m}{X}\Delta Z_2\right)^2 + \left(\frac{Z_2}{X}\Delta S_m\right)^2 + \left(\frac{Z_2 S_m}{X^2}\Delta X\right)^2} \qquad (23)$$

The analysis depends on values for each variable and their respective uncertainties equal to twice its standard deviation. Values for variable K_{eff} and A are calculated from linear regression during calibration and have uncertainties values proportional to the regression's standard error. The value for Z_3 was chosen as 1 V so that the force uncertainty calculated is per 1 V change on the detector. Voltage uncertainty was determined from the standard deviation of position detector data taken at the beginning of the calibration test before the indenter contacted the sample. Similarly, in the indentation calculation, the uncertainty of the tracker position ΔZ_2 was calculated from the standard deviation of the indenter location during contact of the calibration test. The value of Z_2 was chosen to be 108 pixels equivalent to 20 μm representing a conservative value for maximum indentation. The values of S_m and X are taken from the scale of the stage micrometer used to calibrate pixels/μm. The stage micrometer was used to measure a distance of 100 microns with uncertainty of .5 μm. The 100 micron distance was measured 20 times using ImageJ (National Institute of Health), with a mean of 540 pixels and standard deviation of 1.2 pixels. The results are presented in Table 1, with the uncertainty of the force measurement at approximately 0.2830 μN and the uncertainty of the indenter displacement approximately 0.6940 μm.

Table 1 Parameters and results of the uncertainty analysis

	Variable	Uncertainty	Units
Force Measurement	K_{eff}=0.0104	ΔK=0.00042	μN/μm
	A=284.89	ΔA=8.5311	μm/V
	Z_3=1	ΔZ_3=0.01054	V
	F	**ΔF =0.2830**	**μN**

	Variable	Uncertainty	Units
Indenter Displacement	Z_2=108	ΔZ_2=3.6772	pix
	S_m=100	ΔS_m=.5	μm
	X=540	ΔX=2.4	pix
	δ	**Δδ=.6940**	**μm**

2.6 *Discussion*

NTI was used successfully to perform nano-indentation tests on samples of compliant material undergoing adhesive contact. The fiber-optic cantilever used in conjunction with a position detector was capable of supplying force data with a resolution of about 300 nN while optical microscopy aided with tracking software provided displacement data with a resolution of about 700 nm. Using this method, NTI was able to distinguish a ~10 kPa difference in shear modulus between EF30 and EF10 with comparable significance as unconfined compression ($p<0.001$). In addition, the shear moduli obtained using NTI for the two formulations of silicone rubber were consistent with the benchmark values obtained through macroscopic unconfined compression. General agreement between the results of the two test methods is evidenced by the overlapping of the mean±S.D. range for the nano-indentation and benchmark moduli seen for both formulations (Fig 2-12).

The Ogden model used to fit the UC data is a hyperelastic model, while the PT equations used to analyze the NI data are an extension of Hertzian contact and are therefore a linear elastic model. Although Hertzian contact has been modified to accept various nonlinear elastic theories, the technique cannot simultaneously account for general adhesion [45]. To diminish the effect of the hyperelastic nature of the silicone rubber in the NI experiments and to also satisfy the small strain assumption of Hertzian contact, indentation depth was minimized. The theoretical small strain limit of Hertzian contact is a ratio between contact radius a and indenter radius R, $a/R \leq 0.1$. In

application however, this constraint is frequently violated by investigators with experimental and theoretical justification [46,47]. Yoffe reported that Hertz's theory has minimal error in Young's modulus for materials with high Poisson's ratios, a material with v=0.4 has a maximum error in modulus of 1.4% up to an indentation of *a*/R=1. In this study the maximum ratio achieved was *a*/R =.71 indicating an error of approximately 1%.

The NI results analyzed using the PT equations for adhesive contact yielded moduli 13.5% and 20.9% below UC results for EF30 and EF10, respectively. The results seem to show NTI slightly under-predicting the benchmark values, a result that may be caused by any one of several factors. We feel the most likely causes for the underprediction could be inhomogeneity of the hand-mixed silicone samples or surface irregularities existing on the microscale. Small air bubbles close to the indention site would have a greater influence on indentations of a few microns compared to macroscopic compression reaching 25% strain. Another plausible explanation could be due to a limitation of NTI's design; NTI relies on horizontally imaging indentations, which limits the distance from the outer edge of a sample where an indentation can be visualized. The objective utilized for these experiments has a focal length of approximately 3 mm, which allows for approximately 100 indentation radii between the site of indentation and the edge of a sample. In either case, the underprediction for both materials was relatively small, less than the variability from each measurement.

Segments of fiber-optic cable can be turned into cantilevers of variable stiffness by altering the location of an attached microsphere indenter. Although each cantilever's stiffness must be experimentally determined, a relationship has been identified that estimates K_{eff} based on L_{eff} for any cantilever made of stripped AFS-105/125 fiber. Equation 19 predicts a stiffness value of 0.0101 N/m for the cable used in the validation experiments which had an experimentally determined K_{eff}= 0.0104 N/m, a difference of only 3%.

Cantilevers are fairly simple to produce, requiring only a manual fiber-cleaving instrument and a fiber stripper (Newport Corp.). After cleaving a segment of AFS-105/125 cable to a rough length of 10cm, the fiber can be soaked in acetone for 3 minutes to loosen the plastic buffer protecting the cable. The stripper is then used to carefully remove the buffer from the delicate cladding and core. The fiber can then be inserted into the bare fiber holder and attached to the laser. The position table is then used to first bring a bead of epoxy and then a glass microsphere into contact with the fiber at a predetermined location. This process ensures that the microsphere is attached to the bottom of the fiber and will therefore come in contact with a sample. One limitation of the fiber-optic cantilever is the difficulty in repositioning a cantilever so that the indenter is on the bottom of the cable once it has been removed from the fiber holder. Due to this difficulty, it is impractical to pre-fabricate cantilevers of different stiffnesses; thus, cantilevers must be made on-demand.

As a cantilever displacement-controlled device, NTI is not designed for performing testing on time dependent materials due to the coupling of displacement and force. However, a displacement feed-back loop could be implemented to facilitate a constant-force creep test, providing the opportunity to characterize viscoelastic properties of biological materials of interest.

2.7 *Conclusion*

In conclusion, a Nano-Tissue Indenter (NTI) has been developed that can perform nano-indentation testing on biological materials. NTI was validated by comparing its measurements with results obtained through traditional unconfined compression testing, for two formulations of silicone rubber. The device is a displacement-controlled cantilever system that is suited for testing extremely compliant materials and utilizes affordable fiber-optic cable as a measurement tool. Designed with the purpose of investigating the mechanical properties of structures within

the liver, NTI is expected to prove useful for testing a variety of biomaterials in which it is difficult to obtain samples of specific geometry.

Acknowledgments

This research was funded through a Virginia Tech-Wake Forest School of Biomedical Engineering and Sciences Seed Grant (2009-2010) awarded to Dr. Jessica Sparks (PI), Dr. Padma Rajagopalan (Co-PI), and Dr. Raffaella De Vita (Co-PI).

References

1. Gefen A, Margulies SS (2004) Are in vivo and in situ brain tissues mechanically similar? Journal of Biomechanics 37 (9):1339-1352. doi:10.1016/j.jbiomech.2003.12.032

2. Mattice JM, Lau AG, Oyen ML, Kent RW (2006) Spherical indentation load-relaxation of soft biological tissues. Journal of Materials Research 21 (08):2003-2010. doi:doi:10.1557/jmr.2006.0243

3. Yang Y, Bagnaninchi PO, Ahearne M, Wang RK, Liu K-K (2007) A novel optical coherence tomography-based micro-indentation technique for mechanical characterization of hydrogels. Journal of The Royal Society Interface 4 (17):1169-1173. doi:10.1098/rsif.2007.1044

4. Atkins AG, Tabor D (1965) Plastic indentation in metals with cones. Journal of the Mechanics and Physics of Solids 13 (3):149-164. doi:10.1016/0022-5096(65)90018-9

5. Lawn BR (1998) Indentation of Ceramics with Spheres: A Century after Hertz. J Am Ceram Soc 81 (8):1977-1994. doi:10.1111/j.1151-2916.1998.tb02580.x

6. Ebenstein DM, Pruitt LA (2006) Nanoindentation of biological materials. Nano Today 1 (3):26-33. doi:Doi: 10.1016/s1748-0132(06)70077-9

7. Miller K (2005) Method of testing very soft biological tissues in compression. Journal of Biomechanics 38 (1):153-158. doi:10.1016/j.jbiomech.2004.03.004

8. Miller K, Chinzei K (2002) Mechanical properties of brain tissue in tension. Journal of Biomechanics 35 (4):483-490. doi:10.1016/s0021-9290(01)00234-2

9. Oyen ML (2011) Nanoindentation of Biological and Biomimetic Materials. Experimental Techniques:no-no. doi:10.1111/j.1747-1567.2011.00716.x

10. Kemper AR, Santago AC, Stitzel JD, Sparks JL, Duma SM (2010) Biomechanical response of human liver in tensile loading. Ann Adv Automot Med 54:15-26

11. VanLandingham MR (2003) Review of Instrumented Indentation. Journal of Research of the National Institue of Standards and Technology 108 (4):249-265

12. Fischer-Cripps AC (ed) (2002) Nanoindentation. Mechanical Engineering, 2nd edn. Springer, New York

13. Neuman KC, Nagy A (2008) Single-molecule force spectroscopy: optical tweezers, magnetic tweezers and atomic force microscopy. Nat Meth 5 (6):491-505

14. Carpick RW, Salmeron M (1997) Scratching the Surface: Fundamental Investigations of Tribology with Atomic Force Microscopy. Chemical Reviews 97 (4):1163-1194. doi:10.1021/cr960068q

15. Leong PL, Morgan EF (2008) Measurement of fracture callus material properties via nanoindentation. Acta Biomaterialia 4 (5):1569-1575. doi:10.1016/j.actbio.2008.02.030

16. Ferguson VL, Bushby AJ, Boyde A (2003) Nanomechanical properties and mineral concentration in articular calcified cartilage and subchondral bone. Journal of Anatomy 203 (2):191-202. doi:10.1046/j.1469-7580.2003.00193.x

17. Fan Z, Swadener JG, Rho JY, Roy ME, Pharr GM (2002) Anisotropic properties of human tibial cortical bone as measured by nanoindentation. J Orthopaed Res 20 (4):806-810. doi:10.1016/s0736-0266(01)00186-3

18. Ahearne M, Yang Y, El Haj AJ, Then KY, Liu K-K (2005) Characterizing the viscoelastic properties of thin hydrogel-based constructs for tissue engineering applications. Journal of The Royal Society Interface 2 (5):455-463. doi:10.1098/rsif.2005.0065

19. Oliver WC, Pharr GM (1992) An improved technique for determining hardness and elastic modulus using load and displacement sensing indentation experiments. Journal of Materials Research 7 (6):1564-1583. doi:10.1557/JMR.1992.1564

20. Doerner MF, Nix WD (1986) A method for interpreting the data from depth-sensing indentation instruments. Journal of Materials Research 1 (04):601-609. doi:doi:10.1557/JMR.1986.0601

21. Newey D, et al. (1982) An ultra-low-load penetration hardness tester. Journal of Physics E: Scientific Instruments 15 (1):119

22. Bell TJ, et al. (1991) The Determination of Surface Plastic and Elastic Properties by Ultra Micro-indentation. Metrologia 28 (6):463

23. Randall NX, Consiglio R (2000) Nanoscratch tester for thin film mechanical properties characterization. Review of Scientific Instruments 71 (7):2796-2799

24. Kaufman JD, Klapperich CM (2009) Surface detection errors cause overestimation of the modulus in nanoindentation on soft materials. Journal of the Mechanical Behavior of Biomedical Materials 2 (4):312-317. doi:10.1016/j.jmbbm.2008.08.004

25. Houston JE, Michalske TA (1992) The interfacial-force microscope. Nature 356 (6366):266-267

26. Lehenkari PP, Charras GT, Nykänen A, Horton MA (2000) Adapting atomic force microscopy for cell biology. Ultramicroscopy 82 (1-4):289-295. doi:Doi: 10.1016/s0304-3991(99)00138-2

27. Wells RG (2008) The role of matrix stiffness in regulating cell behavior. Hepatology 47 (4):1394-1400. doi:10.1002/hep.22193

28. Discher DE, Janmey P, Wang Y-l (2005) Tissue Cells Feel and Respond to the Stiffness of Their Substrate. Science 310 (5751):1139-1143. doi:10.1126/science.1116995

29. Piersol GA (1916) Normal histology: with special reference to the structure of the human body. J.B. Lippincott Company,

30. Drochmans P, Wanson J-C, Mosselmans R (1975) Isolation and Subfractionation on Ficoll Gradients of Adult Rat Hepatocytes. Size, Morphology, and Biochemical Characteristics of Cell Fractions. The Journal of Cell Biology 66 (1):1-22

31. Levental I, Georges PC, Janmey PA (2007) Soft biological materials and their impact on cell function. Soft Matter 3 (3):299-306

32. Hale NA, Yang Y, Rajagopalan P (2010) Cell Migration at the Interface of a Dual Chemical-Mechanical Gradient. ACS Applied Materials & Interfaces 2 (8):2317-2324. doi:10.1021/am100346k

33. Davidson L, Keller R (2007) Measuring Mechanical Properties of Embryos and Embryonic Tissues. In: YuLi W, Dennis ED (eds) Methods in Cell Biology, vol Volume 83. Academic Press, pp 425-439

34. Lin DC, Dimitriadis EK, Horkay F (2007) Elasticity of rubber-like materials measured by AFM nanoindentation. Express Polym Lett 1 (9):576-584. doi:DOI 10.3144/expresspolymlett.2007.79

35. Popov VL (2010) Contact mechanics and friction physical principles and applications. Springer.

36. Johnson KL, Kendall K, Roberts AD (1971) Surface Energy and the Contact of Elastic Solids. Proceedings of the Royal Society of London A Mathematical and Physical Sciences 324 (1558):301-313. doi:10.1098/rspa.1971.0141

37. Derjaguin BV, Muller VM, Toporov YP (1975) Effect of contact deformations on the adhesion of particles. Journal of Colloid and Interface Science 53 (2):314-326. doi:10.1016/0021-9797(75)90018-1

38. Piétrement O, Troyon M (2000) General Equations Describing Elastic Indentation Depth and Normal Contact Stiffness versus Load. Journal of Colloid and Interface Science 226 (1):166-171. doi:10.1006/jcis.2000.6808

39. Tabor D (1977) Surface forces and surface interactions. Journal of Colloid and Interface Science 58 (1):2-13. doi:10.1016/0021-9797(77)90366-6

40. Maugis D (1992) Adhesion of spheres: The JKR-DMT transition using a dugdale model. Journal of Colloid and Interface Science 150 (1):243-269. doi:10.1016/0021-9797(92)90285-t

41. Ebenstein DM, Wahl KJ (2006) A comparison of JKR-based methods to analyze quasi-static and dynamic indentation force curves. Journal of Colloid and Interface Science 298 (2):652-662. doi:DOI: 10.1016/j.jcis.2005.12.062

42. Ogden RW (1972) Large Deformation Isotropic Elasticity - On the Correlation of Theory and Experiment for Incompressible Rubberlike Solids. Proceedings of the Royal Society of London A Mathematical and Physical Sciences 326 (1567):565-584. doi:10.1098/rspa.1972.0026

43. Shergold OA, Fleck NA, Radford D (2006) The uniaxial stress versus strain response of pig skin and silicone rubber at low and high strain rates. International Journal of Impact Engineering 32 (9):1384-1402. doi:10.1016/j.ijimpeng.2004.11.010

44. Kline S, McClintock F (1953) Describing Uncertainties in Single Sample Experiments. Mechanical Engineering 75 (1):3-8

45. Lin DC, Horkay F (2008) Nanomechanics of polymer gels and biological tissues: A critical review of analytical approaches in the Hertzian regime and beyond. Soft Matter 4 (4):669-682

46. Kumar MV, Narasimhan R (2004) Analysis of Spherical Indentation of Linear Viscoelastic Materials. Current Science 87:1088-1095

47. Yoffe EH (1984) Modified Hertz theory for spherical indentation. Philosophical magazine A 50 (6):813-828

Chapter 3

3. Scale Dependent Mechanical Properties of Native and Decellularized Liver Tissue

D.W. Evans, E.C. Moran, P. Baptista, S. Soker, J.L. Sparks

Scale Dependent Properties of Native and Decellularized Liver Tissue

Douglas W. Evans[1,2], Emma C. Moran[1,2,3], Pedro Baptista[3], Shay Soker[2,3], Jessica L. Sparks[1,2]

1. Department of Biomedical Engineering, Wake Forest School of Medicine
2. Virginia Tech-Wake Forest University School of Biomedical Engineering and Sciences
3. Wake Forest University Institute for Regenerative Medicine

Corresponding Author:
Jessica L. Sparks, Ph.D.
Department of Biomedical Engineering
Wake Forest University School of Medicine
Medical Center Blvd.
Winston Salem, NC 27157
Email: jsparks@wfubmc.edu
Phone: 336-716-4543
Fax: 336-716-5491

Abstract:

Decellularization, one technique used in liver regenerative medicine, is the removal of the native cells from an organ leaving behind an intact structure of extracellular material. The biomechanical properties of this novel scaffold material are currently unknown and are important due the mechanosensitivity of liver cells. Characterizing this material is important for engineering liver tissue from this decellularized scaffold as well as creating new 3-dimensional mimetic structures of liver extracellular matrix. This study set out to characterize the biomechanical properties of perfused liver tissue in its native and decellularized states on both a macro and nano-scale. Poroviscoelastic finite element models were then used to extract the fluid and solid mechanical properties from the experimental data. Tissue-level spherical indentation-relaxation tests were performed on 5 native livers and 8 decellularized livers at two indentation rates and at multiple perfusion rates. Cellular-level spherical nanoindentation was performed on 2 native livers and 1 decellularized liver. Tissue-level results found native liver tissue to possess a Young's modulus of 10.5 kPa and decellularized tissue a modulus of 1.18 kPa. Cellular-level testing found native tissue to have a Young's modulus of 4.40 kPa and decellularized tissue to have a modulus of 0.91 kPa. These results are important for regenerative medicine and tissue engineering where cellular response is dependent on the mechanical properties of the engineered scaffold.

3.1 *Introduction*

Liver diseases including cirrhosis, hepatitis, and hepatocellular carcinoma affect nearly 30 million Americans with organ transplantation as the only long-term treatment currently available [1]. In the United States the number of liver transplantations has been steadily increasing each year reaching 6,291 in 2010 [2]. This number is expected to climb to nearly 8,000 procedures in 2020 [3]. However, the demand for transplantation annually surpasses the supply with the current waiting list at 16,250 [2]. One way to address the deficit in organ supply is through regenerative medicine by creating alternative transplantation materials [4,5].

Decellularization, one technique in regenerative medicine, is the removal of the native cells from an organ leaving behind an intact structure of extracellular material [6]. This technique takes advantage of the native bioactive extracellular matrix (ECM), primarily composed of various types of collagen with embedded signaling proteins, which is necessary to regulate cell differentiation and function. Decellularization also leaves behind an intact de-endothelialized vasculature, which preserves the natural method of supplying cells with blood and oxygen [6]. To recellularize an organ scaffold, perfusion bioreactors are employed to deliver cells and cell culture media back through the intact vasculature [7].

Microvasculature and blood flow are especially important in the liver which at any time holds 10-15% of the body's total supply and receives nearly 30% of the resting cardiac output [8]. In such a vascular organ it is not surprising that parenchymal fluid pressure has recently been shown to affect viability and function of hepatocytes, the primary cell type of the liver [9]. In addition to responding to pressure, hepatocytes have been shown to react to the mechanical environment by altering differentiation and proliferation [10]. Other liver cells including stellate cells, portal fibroblasts, and hepatic stem and progenitor cells have also been shown to exhibit mechanosensitivity and alter behavior based on the stiffness of their substrates [11,12].

Complicating the cellular response to pressure and substrate stiffness is an underlying organ dependent perfusion-stiffness relationship [13].

The mechanosensitivity of the cells populating the liver, and specifically of the cells repopulating a decellularized liver scaffold, highlights the importance of characterizing the biomechanical properties of the scaffold at the cellular scale. In addition, characterizing decellularized liver scaffolds allows for isolation of the matrix contribution to the overall mechanical behavior of the liver. In the emerging field of multi-scale modeling an effort is being made to integrate the small fundamental scales with the large functional scales that exist in the hierarchial structure of biologic systems [14]. While the ECM of the entire liver is a complicated network of interconnected bands of collagen and other proteins, individual cells are only in direct contact with some of these matrix supports and therefore may sense a substrate stiffness much different from the stiffness of the entire organ. To our knowledge, the mechanical properties of decellularized liver tissue have never been reported, for any length scale. To this end, this study set out to characterize the biomechanical properties of perfused liver tissue in its decellularized and native states on both tissue-level and cell-level length scales.

In this work, liver biomechanical properties were quantified using poroviscoelastic constitutive models in finite element simulations of conventional indentation and nano-indentation experiments. The liver is composed of cells embedded on a saturated hydrated porous ECM and is therefore modeled well using poroviscoelasticity (PVE). PVE, a descendant of biphasic theory, has previously successfully been used to model liver tissue[15] as well as brain[16], heart[17], lung[18], cartilage[19], aorta[20], and intervertebral discs[21]. The strength of a PVE model is its ability to simultaneously predict the internal fluid and solid properties of biphasic materials. In this study, we report the development of PVE models for native and decellularized liver at the tissue and cellular scales, using macro and nano-indentation testing of perfused tissue.

3.2 *Materials and Methods*

3.2.1 Experiments

3.2.1.1 Specimens

Liver specimens were obtained from 16 cadaveric ferrets ranging in age from 3-6 weeks. The intact liver was removed through an abdominal incision in which the inferior vena cava, superior vena cava and portal vein were transected while the capsule remained intact. The right lobe was isolated by dissection and the superior vena cava was ligated. The portal vein was cannulated with a 16G cannula, leaving an ex-vivo section of liver tissue with one central input (portal vein) and one output (inferior vena cava). Seven of these samples in this native tissue state were tested within 12 hours of harvest. The remaining 9 ex-vivo sections were then decellularized through perfusion of 1% Triton-X 100 with 0.1% Ammonium Hydroxide (Sigma-Aldrich), as reported by Baptista et al [6]. The decellularized samples were then tested after the decellularization process.

3.2.1.2 Macro-Scale Testing

Macro-indentation experiments were performed on native and decellularized livers using a Bose ElectroForceTestBench mechanical testing system equipped with a 1000-gram load cell (Bose ElectroForce), Fig 3-1. Spherical indenters were created by attaching steel balls (McMaster-Carr) to cup-point set screws (McMaster-Carr) that directly coupled to the load cell. The indenters were 4mm in diameter for the native livers and 8mm in diameter for the decellularized livers. Preliminary results indicated that to maintain an adequate signal to noise ratio, a larger indenter was required to test decellularized liver samples. The livers were supported by a custom articulating drainage platform (Solid Concepts) and attached to a 2-axis manual position system (1/2” dovetail translation stage Thor labs). The setup allowed for liver samples to be perfused with saline using a peristaltic pump (MasterFlex 7523-70 Cole-Parmer) and pulse dampener (Cole-Parmer).

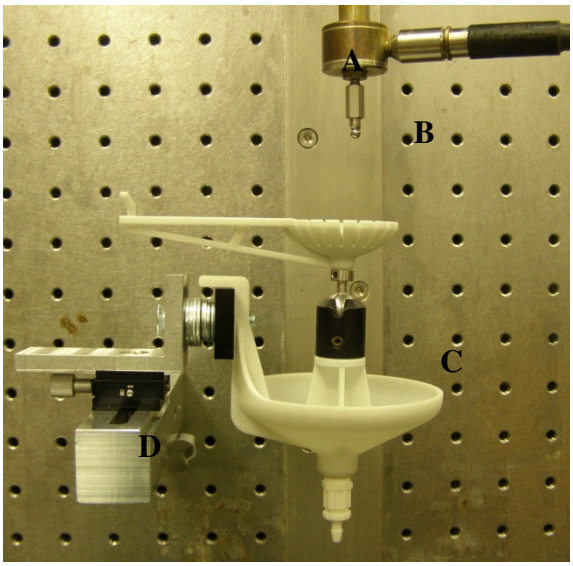

Fig 3- 1: Macro-indentation setup showing: A) load cell, B) spherical indenter and set screw, C) custom-articulating drainage platform, D) 2-axis manual positioner

Macro-indentation tests were performed on 5 of the native and 8 of the decellularized liver samples. For native samples each liver was subjected to 4 tests: 1 test with an indentation rate of 0.01 mm/s perfused with 6 ml/min of saline and 3 tests with an indentation rate of 1 mm/s perfused with 0, 3, and 6 ml/min of saline (Table 3-1). Due to the larger indenter required for the decellularized samples, each decellularized liver was limited to only 2 indentations. Indentation sites on a each sample were spaced approximately 10mm from one another. Decellularized samples were tested under 3 conditions: one test at an indentation rate of 0.01 mm/s perfused with 6 ml/min saline, and 2 tests with an indentation rate of 1 mm/s perfused with 3 and 6 ml/min saline respectively. Five indentations were performed for each of these test conditions totaling 15 decellularized indentations randomly distributed across the 8 samples. For both native and decellularized tests indenter-sample contact was pre-established by a 2 mN load change followed by an indentation of 2mm for native tissue and 4mm for decellularized tissue and 360 s relaxation period.

Table3- 1: Test matrix for macro-indentation showing number of indentations performed

Macro-Indentation				
	Perfusion [ml/min]	**Indentation Rate [mm/s]**		**Indented Surface**
		0.01	**1.0**	
Native	0	---	5	Capsule
	3	---	5	Capsule
	6	5	5	Capsule
Decell	3	---	5	Capsule
	6	5	5	Capsule

3.2.1.3 Nano-Scale Testing

Nano-indentation experiments were performed on native and decellularized livers using a custom cantilever based Nano Tissue Indenter (NTI), Fig 3-2. This device was developed and validated in previous work and can detect applied force and displacement with resolutions of 283 nN and 694 nm [22]. The device uses segments of fiber optic cable to apply a force transmitted through a micro-sphere into a tissue. The force applied is proportional to the cable's stiffness and displacement. Cable stiffness is a function of its length and cable displacement stems from a 3-axis position-table raising a sample into contact with the indenter. The livers were held with the same custom articulating drainage platform as the macro tests. Due to the presence of a fluid film on the surface of the tissue, indenter-sample contact was established by the rest position following "jump-to-contact," the sudden downward pull caused by surface tension of the liquid when the layer is breached. Indentations consisted of raising the livers with a position table at a rate of 0.01 mm/s for 1 mm in the decellularized liver test and 0.05 and 0.01 mm/s for 2 mm in the native liver tests. All NTI based indentations in this study used a titanium indenter with a diameter of 793 μm.

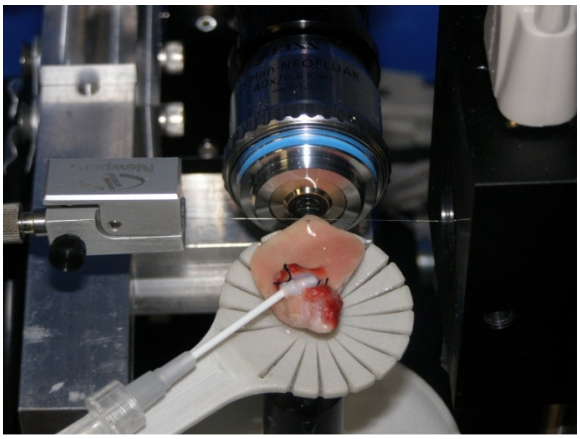

Fig3- 2: Perfused native tissue being nano-indented with NTI

A native liver and decellularized liver both perfused with 6 ml/min of saline were each indented in 10 locations (Table 3-2). Each indentation location was separated by 3 mm and was positioned 10-15 mm from the cannula perfusion source. A cantilever with a stiffness of 0.0183 μN/μm was used for the decellularized indentations and a second cantilever 0.1133 μN/μm stiff was used for the native liver. The stiffer cantilever was necessary after the softer cable failed to indent the native liver a sufficient amount. A second native ferret liver was also tested with the softer cantilever, this time without perfusion. The unperfused native liver was indented 10 times through the capsule and another 7 times in the parenchyma of the tissue after a section of capsule had been removed.

Table3- 2: Test atrix for nano-indentations showing number of indentations performed

		Nano-Indentation		
	Perfusion [ml/min]	**Table Rate [mm/s]**		**Indented Surface**
		0.05	**0.01**	
Native	0	10	---	Capsule
		7	---	Parenchyma
	6	---	10	Capsule
Decell	6	---	10	Capsule

3.2.1.4 Pressure Measurements

A needle guided Millar SPR-524 (3.5F) sensor and MPVS-400 signal conditioning hardware (Millar) with integrated ADInstruments Powerlab DAQ technology were used to measure and record parenchymal fluid pressure in the perfused native and decellularized livers following macro-indentation. The pressure probe was inserted into the same location in 7 decellularized livers and 5 native livers and parenchymal fluid pressure (PFP) was measured at perfusion flow rates of 3ml/min and 6ml/min.

3.2.2 Computational Modeling

3.2.2.1 PVE Theory

PVE theory is an extension of biphasic theory to include an inherent viscoelasticity of the solid component[23]. The underlying biphasic model is a material comprised of a linear elastic incompressible solid and an incompressible liquid where the relative motion between these two phases creates rate-dependent behavior[24]. When the liquid phase is inviscid, biphasic theory has been shown to be equivalent to an alternate theory of a liquid-solid material poroelasticity[25]. Poroelasticity, widely used in soil mechanics, is a material model available in commercial finite-element packages such as Abaqus. The use of Abaqus in modeling soft biphasic tissue has been validated and extended to PVE[15,16,26,27].

The equations governing biphasic theory are given by Eqns 1-6. Under the assumption that the solid phase and fluid phase are both intrinsically incompressible the conservation of mass can be written as:

$$\underline{\nabla} \cdot (\Phi^s \underline{v}^s + \Phi^f \underline{v}^f) = \underline{0} \qquad (1)$$

where s and f stand for solid and fluid phase respectively, Φ is volume ratio, $\underline{v}$ is velocity. Assuming inertial forces to be much smaller in magnitude than internal frictional forces, the conservation of linear momentum can be written as:

$$\underline{\nabla} \cdot \underline{\underline{\sigma}}^s + \underline{\pi}^s = \underline{0} \tag{2}$$

$$\underline{\nabla} \cdot \underline{\underline{\sigma}}^f + \underline{\pi}^f = \underline{0} \tag{3}$$

where $\underline{\underline{\sigma}}$ are Cauchy stress tensors of each phase and $\underline{\pi}$ are frictional body forces (units: F L^{-3}). The frictional body forces are assumed to be proportional to their relative velocities and inversely proportional to the hydraulic permeability k (units: $L^4 F^{-1} T^{-1}$) so that:

$$\underline{\pi}^s = -\underline{\pi}^f = \frac{(\Phi^f)^2}{k}(\underline{v}^f - \underline{v}^s) \tag{4}$$

Finally, the stress in each phase can be written as:

$$\underline{\underline{\sigma}}^f = -\Phi^f p \underline{\underline{I}} \tag{4}$$

$$\underline{\underline{\sigma}}^s = -\Phi^s p \underline{\underline{I}} + \overline{\underline{\underline{\sigma}}}^s \tag{5}$$

where p is hydrostatic pressure and $\overline{\underline{\underline{\sigma}}}^s$ is the apparent solid stress due to deformation of the solid matrix[23-25,27,28]. In PVE theory the effective solid stress tensor $\overline{\underline{\underline{\sigma}}}^s$ is replaced with:

$$\overline{\underline{\underline{\sigma}}}^s = \int_0^t 2G(\tau - \tau') \underline{\underline{\dot{e}}} dt' + \underline{\underline{I}} \int_0^t K(\tau - \tau') \dot{\phi} dt' \tag{7}$$

where G and K are the elastic shear and bulk relaxation functions, $\underline{\underline{e}}$ is the mechanical deviatoric strain and ϕ is the volumetric strain[23,28]. Each relaxation function can be defined by the Prony series expansion:

$$R(t) = \frac{R_\infty}{1 - \sum_{i=1}^{n} r_i} \left[1 - \sum r_i (1 - e^{-t/\tau_i}) \right] \tag{8}$$

where R is the time-dependent modulus, R_∞ is the long-term modulus, and the Prony series parameters (n, r_i, and τ_i, i=1,2,…,n) are material constants[29].

In this work, the material was defined by specifying the hydraulic conductivity (k'), the specific weight of the liquid (γ), Prony series parameters, a long-term Young's modulus (E_∞) and Poisson's ratio (ν) so that:

$$G_\infty = \frac{E_\infty}{2(1+\nu)} \tag{9}$$

$$k = \frac{k'}{\gamma} \tag{10}$$

3.2.2.2 Finite Element Modeling

Macro and nano-scale models of the perfused native and decellularized liver tissue experiments were created in Abaqus (v10.1, Simulia Corp) using its internal soil analysis. The models were axisymmetric and consisted of a sphere indenting a disc of material (Fig 3-3). Since indentation experiments are ideally performed on an infinite half-space [30], the model height and width were 5x and 10x the indenter radii. The indenter was modeled as a deformable solid (type CAX4R) with $E_{ind} >> E_{mat}$. The tissue was modeled as a PVE material using a pore fluid element (type CAX4RP) and by specifying the fluid components (Eqn 10), linear elastic components (Eqn 9), and viscoelastic components (Eqn 8). The model was perfused by specifying the pore pressure on the bottom nodes of the material to match the experimentally measured conditions and allowing the model to equilibrate for 5000 s.

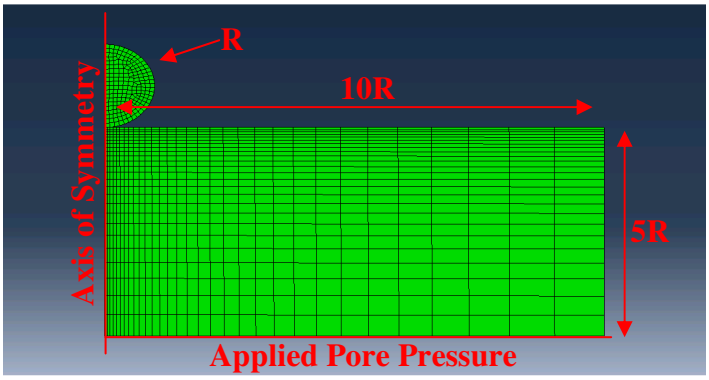

Fig3- 3: Generic finite element axisymmetric indentation model

3.2.2.3 PVE Parameters

The parameters necessary to define a PVE material are the fluid components, elastic components, and viscoelastic components. Fluid components were defined by specifying the hydraulic conductivity of the solid and the specific weight of the fluid. The elastic components were comprised of a long-term Young's modulus and a Poisson's ratio. The viscoelastic components were defined by a multi-term Prony series.

3.2.2.4 Macro-Scale Finite Element Models

The specific weight of the fluid was calculated as the specific weight of saline the perfusion liquid to be 9855 N/m^3. Poisson's Ratio was selected from literature to be 0.35 representing the inherent compressibility of the drained solid matrix [15,16]. The long-term Young's modulus was found by optimizing the model in the absence of viscoelastic terms to match the average fully relaxed force obtained from 6 $^{ml}/_{min}$ perfusion tests. The value for native tissue permeability (k=0.00337 m/s) was deduced from optimization of a PVE model of perfused bovine tissue developed by the authors. While this value is much larger than previously reported values of articular cartilage and other dense soft tissues, it is in the range of estimated permeability of liver as reported in Kerdok *et al* through experimental swelling tests[16,31-33]. The permeability of the decellularized tissue was assumed to be one magnitude larger (k=0.0337 m/s) due to removal of cellular components from the tissue.

The Prony series terms were then found by a two-step process (Appendix). A 4-term Prony series was optimized to the average relaxation experimental data from the samples tested at 1 $^{mm}/_{s}$ with 6 $^{ml}/_{min}$ perfusion using a Hooke-Jeeves algorithm in Isight (v5.2 Simulia Corp). The shear relaxation Prony series function can be viewed in terms of reaction force and assumes that loading has occurred in an instantaneous step occuring at t=0. An approximation to account for actual finite load ramp-time (t_{ramp}) was applied by shifting the relaxation data back by a factor of $t_{ramp}/2$. The first-term components were constrained to g_1=.5 and t_1=2E-5 making up a nearly

instantaneous relaxation component to be used as a scaling variable in the second step. The remaining 3 terms (1 for every decade of relaxation data), were allowed to vary with the constraints in Table 3-3. Because the instantaneous modulus of the material is unknown and depends on the non-unique Prony parameters, a fine tuning of the relaxation parameters is needed to fit model peak force to experimental peak force. Step 2 in the Prony series optimization was manual tuning of the g_1 parameter so the model peak force was within 5% of experimental peak force.

Table3- 3: Constraints on Prony term optimization

Parameters	Constraints	
	min	max
g_2, g_3, g_4	.001	.99
t_1	.01	1
t_2	1	100
t_3	100	1000
$\sum g_n$	.001	.999

3.2.2.5 Nano-Scale Finite Element Models

The identical fluid components, Poisson's ratio, and viscoelastic parameters fit to the macro-scale experimental data were used in the nano-indentation finite element model. The long-term elastic modulus was found by fitting the model force-time curve to the average experimental force-time curve, using the average experimental indentation-time curve as an input.

3.2.3 Statistical Methods

The results were analyzed using two-sample Student's T-tests assuming unequal variance and one-way ANOVAs performed with α=0.05. The Bonferoni method was applied when applicable to avoid compound type 1 error.

3.3 *Results*

3.3.1 Macro-Scale Indentation Experiments

3.3.1.1 Native Livers

The average peak and equilibrium force results are shown for each test group of n=5 in Fig 3-4. Significant differences were found in the three perfusion test groups (0 ml/min, 3 ml/min, and 6 ml/min) indented at 1 mm/s and no significant difference was found between the peak and relaxed force in the slower 0.01 mm/s indentation group. P-values of .0006 for the peak force and .00007 for the equilibrium force indicated that a difference existed within the two force groups. The results show that the indentations performed at 0.01 mm/s with perfusion of 6 ml/min had a statistically significant lower peak force than the indentations performed at 1 mm/s and perfused at 6 and 3 ml/min. No statistical difference could be determined between the mean peak force of the unperfused native liver with any other group due to the large variability in the data. With respect to the mean equilibrium force, the unperfused group was statistically different from the rest of the groups perfused at 3 and 6 ml/min.

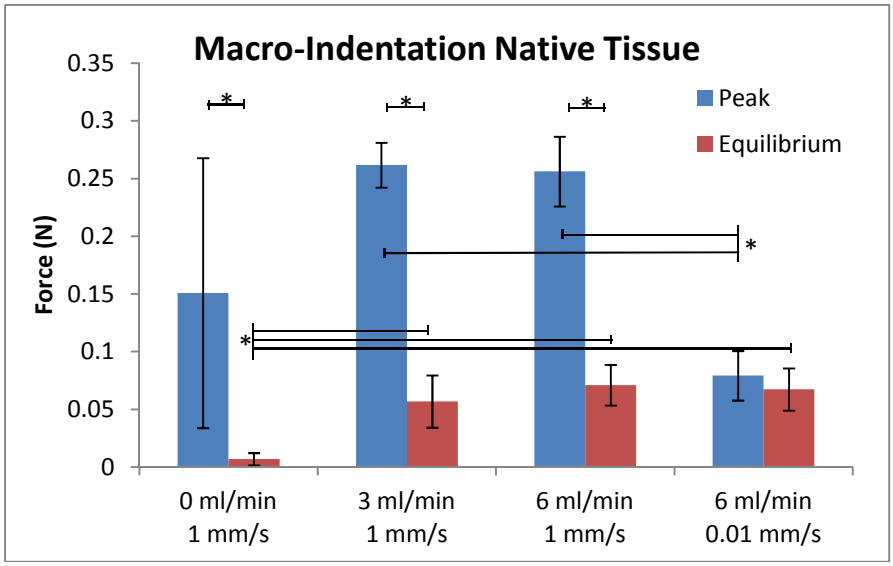

Fig3- 4: Mean peak and equilibrium force from native livers undergoing macro-indentation testing grouped by perfusion and indentation rate. 5 livers were each indented once per perfusion and indentation group totaling 20 indentation tests. A statistical mean difference P<.05 is indicated by (*). Bars indicate ± 1 standard deviation.

3.3.1.2 Decellularized Livers

The mean peak and relaxation force from the 15 macro-indentation tests on 8 decellularized livers are shown in Fig 3-5. A statistical difference between peak and equilibrium force within both test groups indented at 1 mm/s was found with no such difference being detected in the group indented at 0.01 mm/s. P-values of 0.0007 for the mean peak forces and .37198 for the mean equilibrium forces across each group indicated a difference in peak force between groups and no difference in equilibrium force between groups. Further analysis revealed that the peak force from the tests run at the indentation rate of 0.01 mm/s were statistically different from the two tests run at 1 mm/s.

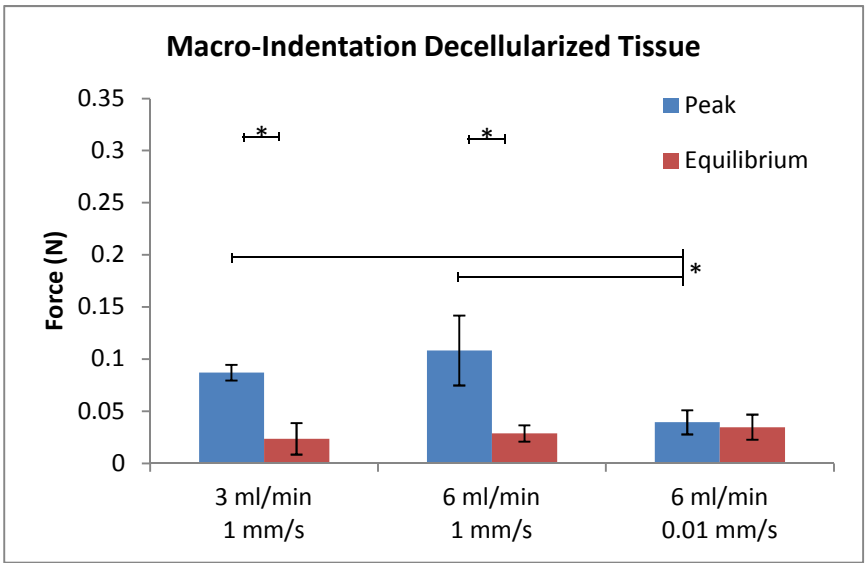

Fig3- 5: Mean peak and equilibrium force from decellularized livers undergoing macro-indentation testing grouped by perfusion and indentation rate. 8 livers were each indented a maximum of 2 times to randomly assigned groups totaling 5 indentations per group. A statistical mean difference P<.05 is indicated by (*). Bars indicate ± 1 standard deviation.

3.3.2 Nano-Scale Indentation Experiments

3.3.2.1 Perfused Samples

The average indentation-force plot stemming from the 10 nano indentation tests performed on a native and decellularized liver are shown in Fig 3-6. The apparent stiffer perfused native liver required a stiffer cantilever than the decellularized tests. All other test conditions including perfusion rate, sample position rate, and indenter size were identical. The peak force and indentation obtained from each material is 108.7 ± 4.1 μN and 74.9 ± 20.6 μm for native liver and 19.0 ± 0.8 μN and 79.6 ± 22.9 μm for decellularized liver. There was no significant difference in indentation depth (p=.6349) but there is a significant difference in the applied force at this depth (p=1.6E-14).

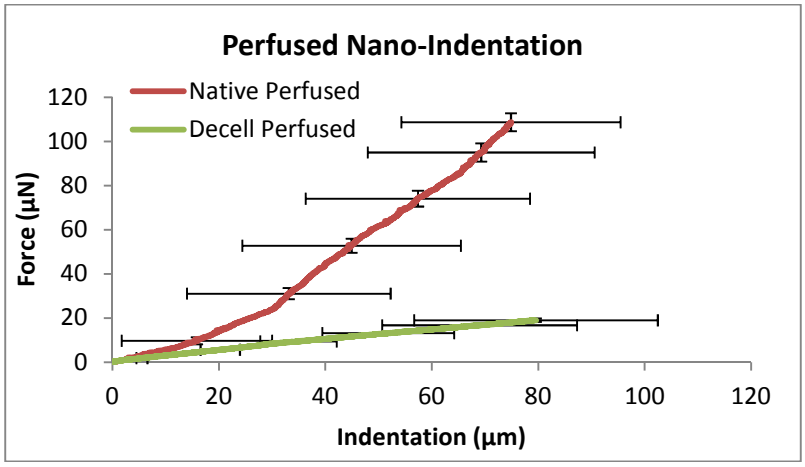

Fig3- 6: Average indentation-force curves for the perfused nano-indentation of native and decellularized liver. The tests were performed with a sample displacement rate of 0.01 mm/s and indentation lasted for 103 seconds.

3.3.2.2 Unperfused Samples

The average indentation-force plot from the 10 tests performed on the capsule and 7 tests in the parenchyma of an unperfused native liver are shown in Fig 3-7. These tests were performed with the identical indenter as the perfused samples; however they used a faster position-table displacement rate. The mean maximum force and indentation for these tests were 38.5 ± 1.2 μN

and 53.9 ± 10.8 µm for the indentations performed through the capsule of the liver and 37.5 ± 0.58 µN and 33.6 ± 8.6 µm for the tests without the capsule of the tissue. There was no signficant difference in the maximum force applied (p=0.12) but again there was a difference found in the indentation (p=0.0006).

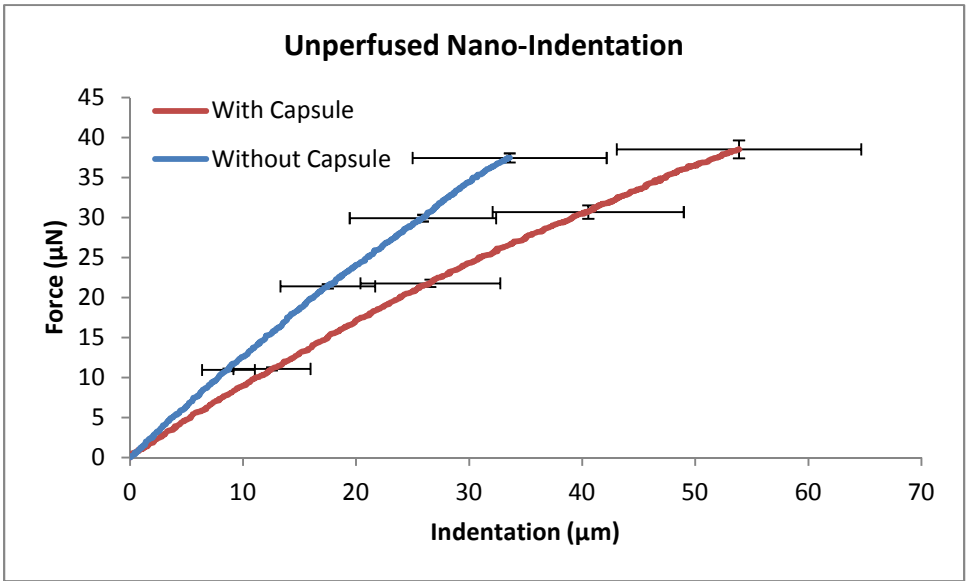

Fig3- 7: Average indentation-force curves for the unperfused nano-indentation of native liver through the capsule and within the parenchyma. The tests were performed with a sample displacement rate of 0.05 mm/s and indentation lasted for 40 seconds.

3.3.3 Pressure Measurements

The results of the pore fluid pressure measurements taken following the macro-indentation tests are shown in Fig 3-8. The mean pore pressures were calculated at each flow rate for both native and decellularized liver tissue. Native tissue had an average pore fluid pressure of 4.32 ± 1.52 mmHg and 7.44 ± 2.49 mmHg for the saline perfusion rates of 3 ml/min and 6 ml/min respectively. Decellularized tissue had an average pore fluid pressure of 0.68 ± 0.53 mmHg and 1.37 ± 0.85 mmHg for the saline perfusion rates of 3 ml/min and 6 ml/min respectively.

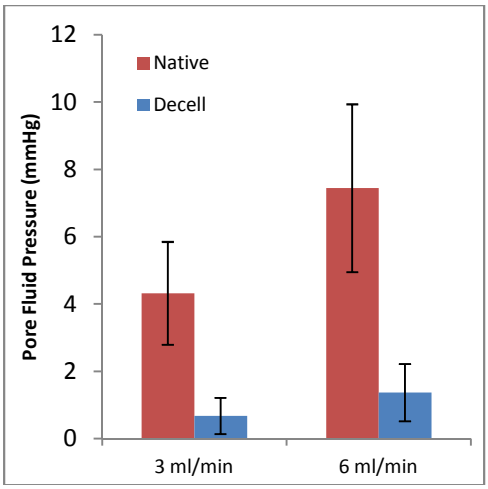

Fig3- 8: The average pore fluid pressure for native (n=5) and decellularized tissue (n=7) when perfused with 3 and 6 ml/min of saline.

3.3.4 PVE Models

3.3.4.1 PVE Parameters

The model parameters for the 6 finite element models created in this study are listed in Table 3-4. The viscoelastic Prony series parameters found from the macro-indentation of native and decellularized tissue were applied to their respective nano-indentation counterparts.

Table 3- 4: Axi-symmetric PVE finite element model parameters

			Elastic Components		Fluid Components		Viscoelastic Components							
		Model	E (kPa)	v	k (m/s)	γ (kg/m³)	g_1	τ_1 (s)	g_2	τ_2 (s)	g_3	τ_3 (s)	g_4	τ_4 (s)
Perfused	Macro	Native	10.5	.35	.00337	9855	.53	2E-5	.376	1	.027	7.65	.01	100
		Decell	1.18	.35	.0337	9855	.481	2E-5	.480	.349	.017	.5	.001	100
	Nano	Native	4.40	.35	.00337	9855	.53	2E-5	.376	1	.027	7.65	.01	100
		Decell	.914	.35	.0337	9855	.481	2E-5	.480	.349	.017	.5	.001	100
Unperfused		Native with Capsule	2.62	.35	.00337	9855	.53	2E-5	.376	1	.027	7.65	.01	100
		Native without Capsule	5.05	.35	.00337	9855	.53	2E-5	.376	1	.027	7.65	.01	100

3.3.4.2 Macro-Indentations

The average force-time tissue response for the native and decellularized macro-indentations perfused at 6 ml/min and their corresponding finite element simulations are shown in Figs 3-9 and 3-10. Native liver tissue was determined to possess a Young's modulus of 10.5 kPa. This value along with the optimized Prony series parameters were simultaneously able to match the peak force (4.89% error) and relaxed force (5.14% error) from the 1 mm/s indentation rate while predicting the peak (3.02% error) and relaxed force (4.82% error) from the slower 0.01 mm/s indentation rate. Decellularized liver was determined to be more compliant with a modulus of 1.18 kPa. The decellularized model matched the peak force (0.40% error) and the relaxed force (8.3% error) for the faster indentation while predicting the slower indentation to 8.3% and 8.5% error respectively for peak and relaxed forces.

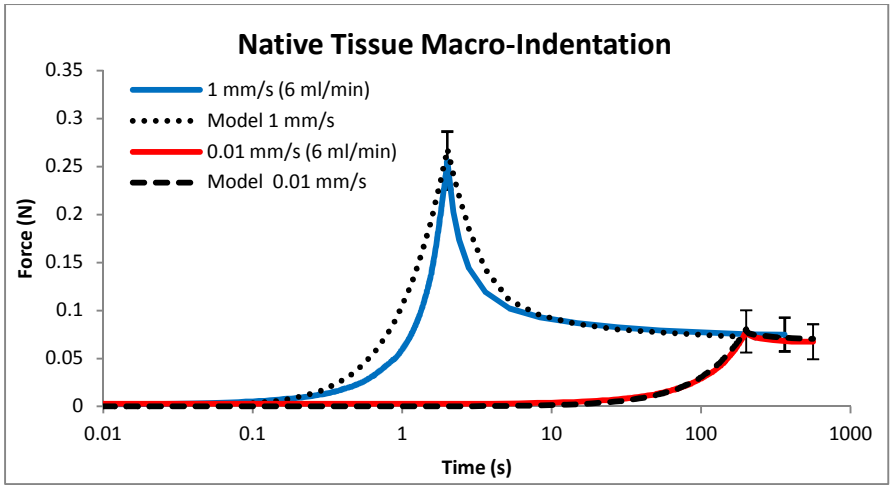

Fig 3- 9: The average experimental tissue and model response from macro-indentations of native liver perfused with 6 ml/min saline.

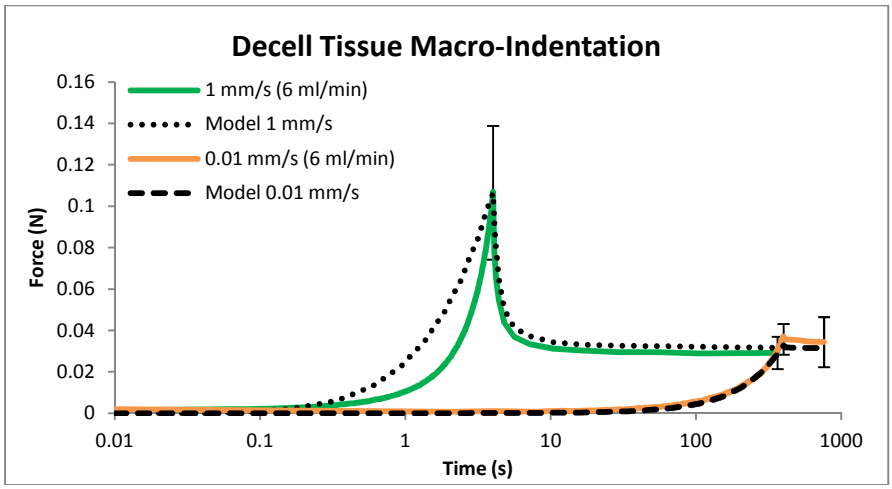

Fig 3- 10: The average experimental tissue and model response from macro-indentations of decellularized liver perfused with 6 ml/min saline.

3.3.4.3 Nano-Indentations

In the four models created to simulate the nano-indentation experiments, the displacement of the indenter was assigned to follow the average indentation-time curve for each group. A Young's modulus was found for each test by minimizing the sum of the residuals squared using a Hookes-Jeeves optimization algorithm (Isight v5.0 Simulia Corp). Figure 3-11 contains 4 force-time plots showing the mean experimental results for each test and the finite element model predictions with corridors indicating the variability in the experimental indention-time data. For the perfused tissue, native liver was found to have a Young's modulus of 4.40 kPa and decellularized liver was found to have a modulus of 914 Pa. The unperfused tests determined native liver with the capsule to have a modulus of 2.62 kPa and native tissue with the capsule removed to have a modulus of 5.05 kPa.

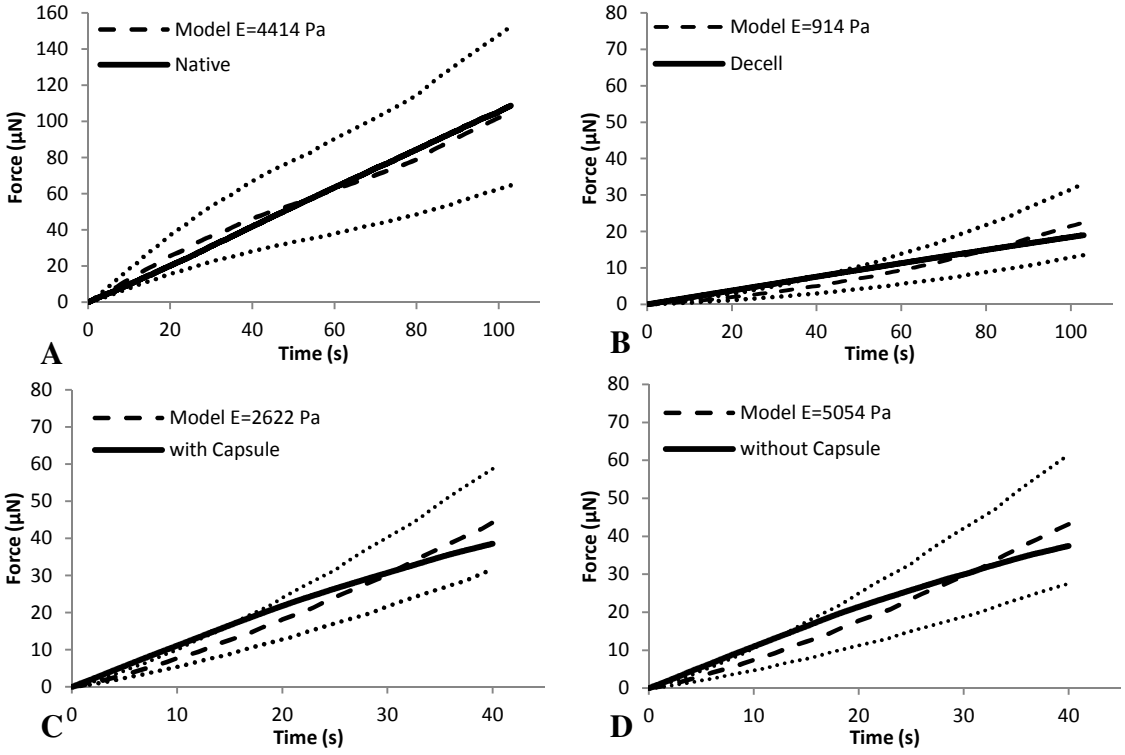

Fig 3- 5: The nanoindentation average experimental force-time data and FE model with corridors representing the variability of the indentation data for: (A) perfused native tissue, (B) perfused decellularized tissue, (C) unperfused native tissue with capsule, and (D) unperfused native tissue without capsule

3.4 *Discussion*

It was found that native and decellularized tissue exhibit different mechanical properties on both the tissue and cellular levels. Macro indentation testing found native perfused liver to possess a Young's modulus of 10.5 kPa and decellularized perfused liver to possess a modulus of 1.18 kPa. Similarly, nanoindentation of the materials also found a difference in the properties with native tissue possessing a Young's modulus of 4.40 kPa and decellularized tissue a value of 0.91 kPa. These findings indicate that the inherent stiffness of liver tissue is lowered significantly from the decellularization process. This result should come as no surprise as the decellularization process removes all of the cellular components leaving behind primarily collagen which makes up 1.8-

2.1% of a normal liver[34]. This is an important finding due to the known mechanosensitivity of liver cells. In the engineering of liver tissue, cells being reseeded and adhering to the decellularized scaffold will therefore be subjected a different mechanical environment than that of native liver. These findings should be taken into account when considering the expected cellular behavior of cells reseeded into a decellularized scaffold.

The change in modulus found for native tissue between macro and nanoindentation was a difference of -58%. This drop in modulus may be partially explained by the number cells the indenter interacted with. The average hepatocyte has a cell diameter of ~30 μm and the maximum contact area of the indentations assuming Hertzian contact was 12.56 mm^2 and 0.201 mm^2 for macro and nanoindention respectively. This means that roughly 17,000 cells were directly contacted by the indenter in macro indentation and only 300 cells in nanoindentation. The Young's modulus of individual liver cells has be reported to be in the range of 1-2.5 kPa as determined by atomic force microscopy[35]. The cellular-scale tests performed in this study are in the upper end of the nanoindentation range and are at a larger scale. It stands to reason that as the scale of the test get closer to testing a single cell, the effective modulus of the cells and their underlying substrate will converge towards the modulus of the single cell. The change in modulus for decellularized tissue was less drastic falling only 23%. While the mechanism for this change in stiffness is unknown, the smaller change in modulus could be due to a similar mechanism as the native tissue. Collagen fibers are inherently smaller than hepatocytes and are made up of individual fibrils with diameters of ~150 nm[36]. Therefore the magnitude of fibers contacted during cellular-level testing could still be significant which could explain the smaller drop in modulus seen in decellularized tissue compared with native tissue.

The macro PVE models fit to the experimental 1 mm/s indentation data were able to simultaneously capture the peak and equilibrium force while predicting the behavior for the slower tests in both native and decellularized tissue. The ramp, or indentation, portion of the

experiments for both native and decellularized tissue exhibit a steeper curvature than the linear elastic PVE indentation model predicts. This discrepancy suggests that the inherent nature of the solid ECM with and without cells maybe better modeled as a hyperelastic material. The solid viscoelastic material properties, the Prony series parameters, show that the native tissue relaxes at a slower rate than the decellularized tissue. The two largest shape-affecting terms of the Prony series (g_2 and g_3) have time coefficients (τ_2 and τ_3) that are both greater than 1 for native tissue and less than 1 for decellularized tissue. The removal of cellular components of the decellularized material is in effect the removal of barriers to fluid flow. Therefore fluid is able to redistribute faster which explains the smaller Prony series time coefficients.

The nanoindentation PVE models were used to determine the Young's moduli of perfused native and decellularized tissue as well as unperfused moduli of indentations occuring on the liver's fibrous capsule and in the parenchyma after the capsule had been removed. The expected findings were that liver parenchyma would be significantly more compliant than the capsulated tissue. The experimental data shows the opposite trend with parenchyma actually being stiffer than both unperfused capsulated tissue and perfused native tissue. One possible explanation of this finding lies in the experimental procedure. After completing the capsule indentations tests, a scalpel was used to remove a section of the tissue exposing the parenchyma. The act of cutting the tissue could have had the unintended effect of squeezing out liquid from the tissue. In this way, the unperfused decapsulated tissue would have behaved like a precompressed material, exhibiting stiffer behavior.

The macro indentation-relaxation of perfused native tissue revealed a difference in reaction force between perfused samples and unperfused samples. The unperfused tissue was anticipated to experience a lower peak and equilibrum force due to absence of a perfusate. This trend was documented in the significant difference seen between the equilibrium force measured between the perfused and unperfused tests. While a significant difference was not found in the

measurement of peak force, the effect of perfusion was seen in the variability of the data. The unperfused peak force variability (0.1508 ± 0.1170 μN) was 4 times the maximum variability seen in the perfused data (0.2562 ± 0.0301 μN), with some samples peaking much lower than the perfused data as expected and surprisingly a few peaking higher than the perfused samples. The elevated peak force measurements are thought to again be an artifact of the experimental procedure. Any pre-test handling of livers has the effect of squeezing fluid out of the tissue, and in the unperfused state this fluid was not replaced before testing. Perfusing the samples therefore had the effect of standardizing each sample, a step which was inherently absent in the unperfused tests.

Although perfusion made a difference in the force measurements, the two rates of perfusion tested in this study did not significantly change peak or equilibrium force for either native or decellularized tissue. Parenchymal fluid pressure measurements taken following macro indentation found the change in pressure between perfusion rates of 3 ml/min and 6 ml/min to be 3.12 and 0.695 mmHg for native and decellularized tissue respectively. The pressure change is the difference in gauge pressure of 72% and 105%, however the pressure actually acting on the tissue is absolute pressure, a difference of only 0.4% and 0.09%. The small actual change in absolute pressure may explain the absence of a reaction force dependence on flow-rate.

The time-dependent nature of native and decellularized tissue was confirmed by the results of the 2 indentation rates. The slower rate of 0.01 mm/s did not produce a significant difference in peak force compared with equilibrium force while the faster rate of 1 mm/s did produce a significant difference, between peak and equilibrium force for both native and decellularized tissue.

3.5 *Conclusion*

In conclusion, this work reports the difference in the mechanical properties between perfused decellularized and native liver on both the tissue and cellular scale. These results are relevant for

regenerative medicine and tissue engineering where cellular response is dependent on the mechanical properties of the engineered scaffold. In addition, PVE models were successfully created that modeled and predicted spherical macro and nanoindentation response. The strength of the PVE model is its ability to separate yet integrate the solid and fluid components of a biphasic material. This is particularly important in modeling biologic tissue such as the liver where perfusion plays an important role in the physiologic and mechanical response.

References

1. Uygun BE, Soto-Gutierrez A, Yagi H, Izamis ML, Guzzardi MA, Shulman C, Milwid J, Kobayashi N, Tilles A, Berthiaume F, Hertl M, Nahmias Y, Yarmush ML, Uygun K (2010) Organ reengineering through development of a transplantable recellularized liver graft using decellularized liver matrix. Nature medicine 16 (7):814-820

2. OPTN (2011) Organ Procurement and Transplantation Network: National Data. http://optn.transplant.hrsa.gov/. Accessed November 1 2011

3. Scarborough JE, Tuttle-Newhall JE, Pietrobon R, Marroquin CE, Collins BH, Desai DM, Kuo PC, Pappas TN (2008) Supply and demand for liver transplant surgery: Are we training enough surgeons? HPB 10 (1):25-29. doi:10.1080/13651820701883098

4. Orlando G, Wood KJ, Stratta RJ, Yoo JJ, Atala A, Soker S (2011) Regenerative Medicine and Organ Transplantation: Past, Present, and Future. Transplantation 91 (12):1310-1317 1310.1097/TP.1310b1013e318219ebb318215

5. Orlando G, Baptista P, Birchall M, De Coppi P, Farney A, Guimaraes-Souza NK, Opara E, Rogers J, Seliktar D, Shapira-Schweitzer K, Stratta RJ, Atala A, Wood KJ, Soker S (2011) Regenerative medicine as applied to solid organ transplantation: current status and future challenges. Transplant International 24 (3):223-232. doi:10.1111/j.1432-2277.2010.01182.x

6. Baptista PM, Siddiqui MM, Lozier G, Rodriguez SR, Atala A, Soker S (2011) The use of whole organ decellularization for the generation of a vascularized liver organoid. Hepatology 53 (2):604-617. doi:10.1002/hep.24067

7. Martin I, Wendt D, Heberer M (2004) The role of bioreactors in tissue engineering. Trends in Biotechnology 22 (2):80-86. doi:10.1016/j.tibtech.2003.12.001

8. Guyton AC, Hall JE (2006) Textbook of medical physiology. Elsevier Saunders, Philadelphia, Penns.

9. Hsu W-M, Carraro A, Kulig KM, Miller ML, Kaazempur-Mofrad M, Weinberg E, Entabi F, Albadawi H, Watkins MT, Borenstein JT, Vacanti JP, Neville C (2010) Liver-Assist Device With a Microfluidics-Based Vascular Bed in an Animal Model. Annals of Surgery 252 (2):351-357 310.1097/SLA.1090b1013e3181e1982ba

10. Hansen LK, Wilhelm J, Fassett JT (2005) Regulation of Hepatocyte Cell Cycle Progression and Differentiation by Type I Collagen Structure. In: Gerald PS (ed) Current Topics in Developmental Biology, vol Volume 72. Academic Press, pp 205-236

11. Wells RG (2008) The role of matrix stiffness in regulating cell behavior. Hepatology 47 (4):1394-1400. doi:10.1002/hep.22193

12. Lozoya OA, Wauthier E, Turner RA, Barbier C, Prestwich GD, Guilak F, Superfine R, Lubkin SR, Reid LM (2011) Regulation of hepatic stem/progenitor phenotype by microenvironment stiffness in hydrogel models of the human liver stem cell niche. Biomaterials 32 (30):7389-7402. doi:10.1016/j.biomaterials.2011.06.042

13. Kerdok AE, Ottensmeyer MP, Howe RD (2006) Effects of perfusion on the viscoelastic characteristics of liver. Journal of Biomechanics 39 (12):2221-2231. doi:10.1016/j.jbiomech.2005.07.005

14. Markus J B (2011) Multiscale aspects of mechanical properties of biological materials. Journal of the Mechanical Behavior of Biomedical Materials 4 (2):125-127. doi:10.1016/j.jmbbm.2010.12.018

15. Raghunathan S, Evans D, Sparks J (2010) Poroviscoelastic Modeling of Liver Biomechanical Response in Unconfined Compression. Ann Biomed Eng 38 (5):1789-1800. doi:10.1007/s10439-010-9957-x

16. Cheng S, Bilston LE (2007) Unconfined compression of white matter. Journal of Biomechanics 40 (1):117-124. doi:10.1016/j.jbiomech.2005.11.004

17. Ng EYK, Ghista DN, Jegathese RC (2005) Perfusion studies of steady flow in poroelastic myocardium tissue. Computer Methods in Biomechanics and Biomedical Engineering 8 (6):349-357. doi:10.1080/10420150500433044

18. Pitt Ford TR, Sachs JR, Grotberg JB, Glucksberg MR (1991) Perialveolar interstitial resistance and compliance in isolated rat lung. Journal of Applied Physiology 70 (6):2750-2756

19. DiSilvestro MR, Zhu Q, Suh J-KF (2001) Biphasic Poroviscoelastic Simulation of the Unconfined Compression of Articular Cartilage: II---Effect of Variable Strain Rates. Journal of Biomechanical Engineering 123 (2):198-200

20. Ayyalasomayajula A, Geest JPV, Simon BR (2010) Porohyperelastic Finite Element Modeling of Abdominal Aortic Aneurysms. Journal of Biomechanical Engineering 132 (10):104502

21. Yang Z, Smolinski P (2006) Dynamic finite element modeling of poroviscoelastic soft tissue. Computer Methods in Biomechanics and Biomedical Engineering 9 (1):7-16. doi:10.1080/10255840500529540

22. Evans DW, Rajagopalan P, Devita R, Sparks JL (2011) Compression instrument for tissue experiments (cite) at the meso-scale: device validation - biomed 2011. Biomed Sci Instrum 47:264-269

23. Mak AF (1986) The Apparent Viscoelastic Behavior of Articular Cartilage---The Contributions From the Intrinsic Matrix Viscoelasticity and Interstitial Fluid Flows. Journal of Biomechanical Engineering 108 (2):123-130

24. Mow VC, Kuei SC, Lai WM, Armstrong CG (1980) Biphasic Creep and Stress Relaxation of Articular Cartilage in Compression: Theory and Experiments. Journal of Biomechanical Engineering 102 (1):73-84

25. Simon BR (1992) Multiphase Poroelastic Finite Element Models for Soft Tissue Structures. Applied Mechanics Reviews 45 (6):191-218

26. Wu JZ, Herzog W, Epstein M (1997) Evaluation of the finite element software ABAQUS for biomechanical modelling of biphasic tissues. Journal of Biomechanics 31 (2):165-169. doi:10.1016/s0021-9290(97)00117-6

27. DiSilvestro MR, Zhu Q, Wong M, Jurvelin JS, Suh J-KF (2001) Biphasic Poroviscoelastic Simulation of the Unconfined Compression of Articular Cartilage: I---Simultaneous Prediction of Reaction Force and Lateral Displacement. Journal of Biomechanical Engineering 123 (2):191-197

28. Suh J-K, Bai S (1998) Finite Element Formulation of Biphasic Poroviscoelastic Model for Articular Cartilage. Journal of Biomechanical Engineering 120 (2):195-201

29. Abaqus (2010) ABAQUS User's Manual (Version 6.10)

30. Johnson KL, Kendall K, Roberts AD (1971) Surface Energy and the Contact of Elastic Solids. Proceedings of the Royal Society of London A Mathematical and Physical Sciences 324 (1558):301-313. doi:10.1098/rspa.1971.0141

31. Gu WY, Mao XG, Foster RJ, Weidenbaum M, Mow VC, Rawlins BA (1999) The Anisotropic Hydraulic Permeability of Human Lumbar Anulus Fibrosus: Influence of Age, Degeneration, Direction, and Water Content. Spine 24 (23):2449

32. Mansour JM, Mow, Van C. (1976) The Permeability of Articular Cartilage Under Compressive Strain and at High Pressures. The journal of Bone and Joint Surgery 58 (4):509-516

33. Kerdok AE (2006) Characterizing the nonlinear mechanical response of liver to surgical manipulation.

34. Aycock RS, Seyer JM (1989) Collagens of normal and cirrhotic human liver. Connect Tissue Res 23 (1):19-31

35. Cross SE, Jin Y-S, Rao J, Gimzewski JK (2007) Nanomechanical analysis of cells from cancer patients. Nat Nano 2 (12):780-783. doi:http://www.nature.com/nnano/journal/v2/n12/suppinfo/nnano.2007.388_S1.html

36. Hay ED (1991) Cell biology of extracellular matrix. Plenum Press,

Appendix

Prony Series Optimization

A multi-term Prony series, as used in ABAQUS, can describe how the shear modulus of a viscoelastic material changes with time. A Prony series term consists of a non-dimensional coefficient paired with a time constant. The number of terms is usually equal to the number of logarithmic decades that experimental relaxation spans. The terms are calculated by some optimization process fitting the function to experimental relaxation data. The Prony series can be written to be based on a materials instantaneous modulus (Eqn A.1) or in the more useful form (when stress-relaxation data is available) based on a materials long-term equilibrium modulus (Eqn A.2).

$$G(t) = G_0\left(1 - \sum g_i(1 - e^{-t/\tau_i})\right) \tag{A.1}$$

$$G_0 = \frac{G_\infty}{1 - \sum g_i} \tag{A.2}$$

In this work, the contact area following indentation ($t > t_{ramp}$) and the Poisson's ratio of the material are assumed to be constant. Therefore Eqns A.1 and A.2 can be written to predict how force changes with time based on the long-term equilibrium force.

$$F(t) = F_0\left(1 - \sum g_i(1 - e^{-t/\tau_i})\right) \tag{A.3}$$

$$F_0 = \frac{F_\infty}{1 - \sum g_i} \tag{A.4}$$

The result of a direct fitting of a Prony series to relaxation data ($t > t_{ramp}$) is shown in Fig A.1. Plotted on the figure are the linear elastic response and the viscoelastic response of a material with the same instantaneous elastic modulus to a compression lasting tramp seconds. As the graph shows the fit Prony series matches the relaxation data very well, except the specific

parameters significantly over predicts the true instantaneous force that would be exhibited by the material. It is important to note that this specific set of Prony series parameters fitting the relaxation data is not unique and that the predicted instantaneous force can vary considerably based on the specific solution due to the denominator in Eqn A.4 .

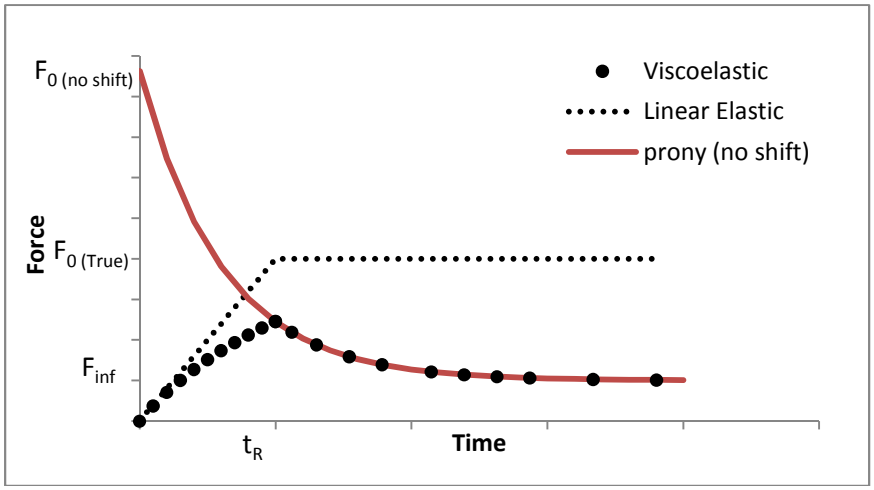

Fig A. 1: The linear elastic and viscoelastic behavior of a material with the same instantaneous modulus and the optimized Prony series prediction

An approximation devised to limit the magnitude of this overestimation is to shift the experimental data back by ½ t_{ramp} (Fig A.2). Because of the finite ramp-time in experimental data, a viscoelastic material is actually relaxing as load is being applied. The Prony series by itself cannot account for this finite ramp-time, therefore any predicted relaxation curves are not going to perfectly match FE results. To address this issue, the idea of an artifical scaling term was devised to adjust the optimized Prony series parameters.

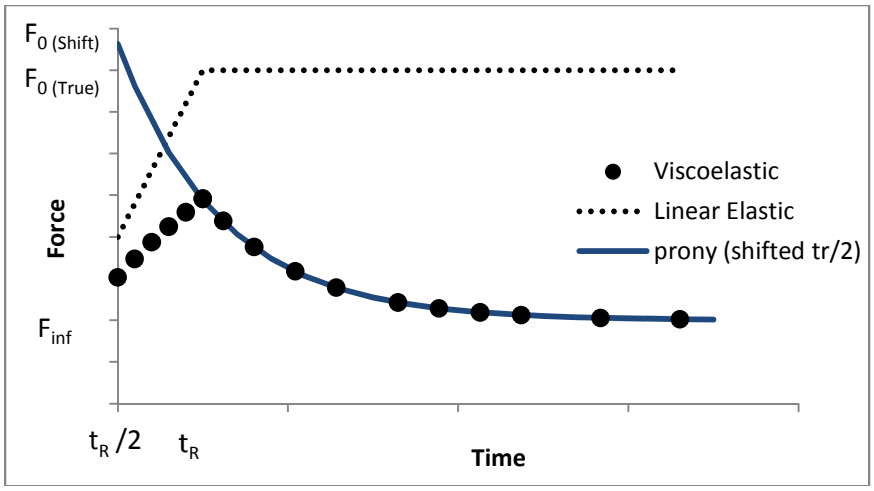

Fig A. 2: The optimized Prony series prediction following an experimental time shift of tramp/2

It can be seen from Eqn A.2 that the instantaneous modulus is only dependent on the non-dimensional coefficients of the Prony parameters and not the time coefficients. Therefore in order to adjust the peak force predicted in the model a g_i term could be raised to increase the effective instantaneous modulus or lowered to decrease it. In this process, to avoid altering the shape of the relaxation curve the g_i parameter altered should be associated with small time coefficient so that the viscoelastic effects described by that term dissipate very quickly. To implement this plan, an additional Prony series term was added with the arbitrary non-dimensional value of g_1=.5 and a time coefficient $<<t_{ramp}$, τ_1=2E-5. Following the fitting of the Prony series with this artifical scaling term to relaxation data, the relaxation function was evaluated by simulating the experiment with a FE model. The peak model force could then be tailored to agree with the peak experimental force by adjusting the g_1 parameter without significantly effecting the shape of the relaxation curve.

Chapter 4:

4. Conclusion

Regenerative medicine, in particular the tissue engineering of whole livers, has the potential to be a viable solution to the massive organ donor shortage. However, for the successful engineering of liver tissue, it is very important to consider the biomechanical environment in which the cells are interacting. This is important not only for the reseeding of decellularized liver matrices, but also in the development of new tissue engineered materials that mimic the extracellular matrix. Currently reasearch on liver tissue being conducted in regenerative medicine is lacking knowledge of the mechanical properties of the engineered decellularized scaffolds. By characterizing these properties, researchers will now be able to adapt to matrix stiffness differences in native versus decellularized liver and research the effects that these differences may have on cell mechanosensitivity. This research could also lead to optimization of the re-seeding process to successfully engineer functional liver tissue, or in the development of new tissue engineered alternatives.

The successful development and validation of NTI allows for affordable multi-scale indentation tests to be performed on virtually any soft biologic tissue or biomaterial. The device takes advantage of two independent measurements to provide accurate force data with resolution of 283 nN and indentation data at 694 nm. The design also allows for future improvements such as additional microscope objectives and various attachments to allow for a vast array of testing requirements such as perfusion.

The testing of perfused native and decellularized liver on the tissue and cellular-scales are important contributions to the emerging fields of regenerative medicine and multi-scale modeling. This biomechanical characterization of decelluarized liver tissue scaffold is the first of its kind and will be useful in the development of alternative tissue mimetics. The PVE model employed to

determine the mechanical properties of the tissue is a powerful tool for studying the complex mechanics of hydrated soft tissue.

In the future, it would make sense to continue this line of testing to decellularized scaffolds at various stages of recellulariztion to quantify how the scaffold stiffens with the adhesion of live cells. There is also benefit to extending this work to even smaller scales to explore variations of ECM properties across microstructures within the liver. The further development of predictive PVE finite element models would also be beneficial.

Chapter 5

5. Scholastic Vita

Douglas W. Evans

Douglas.W.Evans@gmail.com

EDUCATION

Virginia Tech-Wake Forest University School of Biomedical Engineering Sciences
Winston-Salem, NC - Masters Degree in Biomedical Engineering (Exp: December 2011)*, August 2009-Present*

Temple University
Philadelphia, PA – Bachelors of Science in Mechanical Engineering*, Jan 2007-May 2009*

Bucks County Community College
Newtown, PA – Associates of Arts in Mathematics, *Aug 2006 – Jan 2007*

Pennsylvania State University
State College, PA – Engineering, History, Enviromental Science, Aug 2001 – May 2005

BIBLIOGRAPHY

Papers in Refereed Publications

1. Raghunathan S, Evans D, Sparks J (2010) Poroviscoelastic Modeling of Liver Biomechanical Response in Unconfined Compression. Ann Biomed Eng 38 (5):1789-1800. doi:10.1007/s10439-010-9957-x
2. Evans DW, Rajagopalan P, Devita R, Sparks JL (2011) Compression instrument for tissue experiments (CITE) at the meso-scale: device validation - biomed 2011. Biomed Sci Instrum 47:264-269
3. Evans DW, Vavalle NA, De Vita R, Rajagopalan P, Sparks JL (Under Review) Nano-Indentation Device for Investigating the Biomechanics of Liver Extracellular Matrix

Conference papers (abstract style or non-refereed)

1. SBES 2010
2. BMES 2010.
3. RMBS 2011.
4. SBES 2011

Conferences and Presentations

1. Invited Oral Presenter, Virginia Tech-Wake Forest University School for Biomedical Engineering and Sciences Research Symposium, Blacksburg, VA, 2011.
2. Invited Oral Presenter, RMBS, Denver, CO, 2011
3. Invited Poster Presenter, BMES Conference, Austin, TX, 2010.

4. Invited Poster Presenter, Virginia Tech-Wake Forest University School for Biomedical Engineering and Sciences Research Symposium, Winston-Salem, NC, 2010.

SKILLS

Abaqus	C++	Mimics
Ansys Workbench	Java	LabVIEW
AutoCAD	Matlab	Simulink
Bose Electroforce Test Bench	Microsoft Office	Visual Basic

PROFESSIONAL MEMBERSHIPS

BMES 2009 – Present

IEEE (EMBS) 2009 – Present